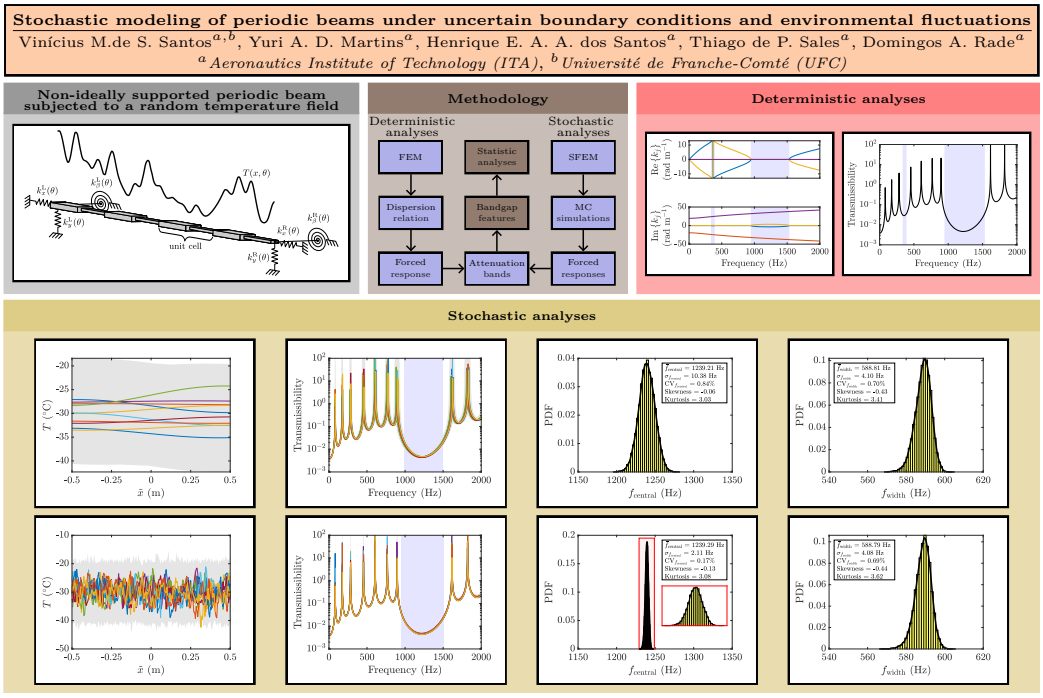
Graphical Abstract

Stochastic modeling of periodic beams under uncertain boundary conditions and environmental fluctuations

Vinícius M. de S. Santos, Yuri A. D. Martins, Henrique E. A. A. dos Santos, Thiago de P. Sales, Domingos A. Rade



Highlights

Stochastic modeling of periodic beams under uncertain boundary conditions and environmental fluctuations

Vinícius M. de S. Santos, Yuri A. D. Martins, Henrique E. A. A. dos Santos, Thiago de P. Sales, Domingos A. Rade

- One considers thermal and BC uncertainties in the stochastic model of a periodic beam
- Both uncertainty sources are relevant to the characteristics of attenuation bands
- Central frequency is mostly influenced by temperature, and bandwidth mainly by BCs
- Response variability depends on the interplay of CVs and temperature correlation length
- Larger correlation length and CVs yield the lowest reliability

Stochastic modeling of periodic beams under uncertain boundary conditions and environmental fluctuations

Vinícius M. de S. Santos[a,b], Yuri A. D. Martins[a], Henrique E. A. A. dos Santos[a], Thiago de P. Sales[a], Domingos A. Rade[a,*]

[a]*Mechanical Engineering Division, Aeronautics Institute of Technology, Praça Marechal Eduardo Gomes, 50 - Vila das Acácias, São José dos Campos, 12228-900, SP, Brazil*
[b]*SUPMICROTECH, Université de Franche-Comté, CNRS, Institut FEMTO-ST, Besançon, F-25000, Doubs, France*

Abstract

Periodic structures have been attracting a great deal of academic and industrial interest lately, due to their distinctive vibration and wave propagation behavior, which can be explored for the development of innovative solutions to structural dynamics and vibroacoustic problems. Although such a potential has been demonstrated in a large number of studies, the investigation of detrimental effects, which can be present in practical applications, is still necessary. This paper reports investigations on the combined influence of uncertainties affecting ambient temperature — which alters material properties and induces stress-stiffening due to constrained thermal dilatation — and boundary conditions (BCs) on the bandgap characteristics of periodic beams. The space-dependent temperature fluctuations are represented as a one-dimensional stationary Gaussian random field, discretized using the Karhunen-Loève expansion, while non-ideal BCs, represented as springs, are modeled as discrete random variables. Sampling-based stochastic analyses of the central frequency and bandwidth of the beam's attenuation bands are performed using Monte Carlo simulations. The results demonstrate that the variability in the attenuation band features is influenced not only by the coefficients of variation (CVs) of the input random quantities, but also by the

*Corresponding author
Email addresses: vinicius.santos@ga.ita.br (Vinícius M. de S. Santos), yurimartins@ita.br (Yuri A. D. Martins), henrique.almada@ga.ita.br (Henrique E. A. A. dos Santos), tpsales@ita.br (Thiago de P. Sales), domingos.rade@gp.ita.br (Domingos A. Rade)

correlation length of the random temperature fluctuations. Numerical simulations reveal that the bandgap central frequency is primarily affected by the temperature random field, while the BCs govern the bandwidth. Although low CV and standard deviation values are obtained for the dispersion of the bandgap features, reliability analyses indicate that some designs exhibit low reliability. Increased variability in both the bandgap central frequency and bandwidth is observed for greater temperature correlation lengths and CVs. The contributions of the study include the proposal of a comprehensive stochastic modeling procedure duly accounting for relevant random influences, and evidencing that those influences can be significant, requiring consideration in the design of robust periodic structures.

Keywords: periodic structures, thermo-elastodynamics, uncertainty quantification, bandgap, uncertain boundary conditions, reliability analysis

1. Introduction

In the field of structural dynamics, periodic structures are understood as those constituted by the coupling of identical substructures, known as *unit cells*, which are repeated along one, two or three directions. Those structures have attracted the interest of the scientific community in the last decades, especially due to the possibility they offer for shaping elastic vibrations and wave propagation patterns [1–3]. Of particular interest is the occurrence of the so-called *attenuation bands*, sometimes interchangeably referred to as *bandgaps* or *stop bands*. These attenuation bands are frequency ranges where the propagation of elasto-acoustic waves cannot occur. This phenomenon can result from destructive interference of propagating and reflected waves due to the periodic mismatch of mechanical impedances (*Bragg scattering*). Periodic structures presenting this effect are also called *phononic crystals* (PCs). In addition, attenuation bands can be achieved by the introduction of resonating subsystems into the unit cells, thus characterizing the so-called *locally resonant* periodic structures or *elastic metamaterials*. In both cases, the underlying phenomena can be explored to achieve vibration attenuation, besides a number of other interesting effects not observed in ordinary structures [4–7].

The literature abounds with research papers devoted to periodic structures, addressing their phenomenology, modeling and experimental characterization, also demonstrating their potential for the development of inno-

vative solutions to engineering problems in structural dynamics and vibroacoustics [8–11]. However, contrarily to the theoretical assumptions, perfect periodicity is seldom possible in practice. Structures whose periodicity deviates from the ideal one are referred to in the literature as *nearly-periodic*, *quasi-periodic* or *disordered* [12–15]. Periodicity can be broken by the occurrence of defects localized in one or more unit cells, limitations of manufacturing processes (e.g., geometric tolerances, induced residual stresses) and/or variability of material properties. These latter result from uncertainties affecting some key factors intervening in material processing, such as chemical composition and environmental conditions.

As a consequence of environmental influences, structural systems may vary their mechanical behavior [16, 17]. In fact, it is known that temperature fluctuations can exert strong influence on the static and dynamic behavior of structural components, which can be explained by two main effects: a) the dependence of physical parameters (e.g. elastic moduli) on temperature, due to influences at the atomic or molecular levels; and b) the variation of the apparent stiffness of structures (especially slender beam-like and plate-like components), due to the occurrence of the so-called *stress-stiffening effect* [18, 19]. When it comes to polymer-matrix composite materials, not only temperature, but also humidity, can exert significant influence on their mechanical behavior [20].

Other relevant sources of uncertainty in structural dynamics are boundary conditions (BCs). Most often, structural models assume perfect supports (free, pinned, clamped, sliding, etc.), while, in practice, most types of constraining devices and connections can hardly reproduce ideal constraints, such as null rotations and displacements in clamped sections [21]. In fact, actual connections and supports, frequently make use of bolted, riveted and welded joints, thus possessing certain degree of flexibility, which depends on geometry, material properties and manufacturing/assembling tolerances [22–25]. In addition, contacting surfaces in bolted joints can undergo stick-slip phenomena, which induce energy dissipation and nonlinear behavior [26]. As shown in ref. [27], considerable improvements could be obtained in the agreement between experimental and theoretical dynamic responses of beam-like structures by taking into account the rotational flexibility of the BCs. A comparison between experimental and predicted dynamic results of a beam with non-ideal BCs was conducted in [28] as well, highlighting the importance of incorporating non-ideal clamp boundaries in the modeling of nonlinear vibrations of a clamped-clamped steel beam. Furthermore, the nonlinear dynamic

behavior of beams accounting for imperfections in BCs was investigated in [29] by resorting to stochastic methods.

All the variabilities mentioned above can hardly be controlled and characterized at affordable cost. Their consideration in the scope of fully deterministic approaches would be very complex, possibly involving convoluted multi-physical and multi-scale techniques. As a result, an alternative route for their consideration has been developed in which the variabilities are rationally accounted for in the context of the so-called *non-deterministic approaches*, among which the category of probabilistic techniques has gained considerable maturity and popularity lately [30, 31]. The imperative for dealing with uncertainties intervening in complex systems (not only those found in Engineering, but also in a variety of domains) has led to the emergence of a field of knowledge known as *Uncertainty Quantification* (UQ) [32, 33].

Most previous research works have addressed the variabilities mentioned above. Minghui Zhang and co-authors recently considered manufacturing imperfections during the bandgap optimization of stochastic elastic metamaterials [34]. Ribeiro et al. [35] conducted a robust optimization scheme for designing three-dimensional printed periodic frame structures accounting for manufacturing variability. Al Ba'ba'a et al. [36] studied possible issues due to the same source of variability and how they may provoke deviations from theoretical predictions. Manufacturing uncertainties were further assessed concerning the variability of additively manufactured metastructures [37, 38], and in identifying wavenumber variations in metamaterial beams [39]. Chatterjee and collaborators [40] investigated the dynamic response of a periodic beam under random geometrical and material uncertainties to simulate manufacturing variabilities represented by a log-normal distribution. Uncertainties in material properties and geometry were also addressed to develop a topology optimization scheme for auxetic [41] and mechanical [42, 43] metamaterials. Geometric variabilities were likewise approached to design three-dimensional periodic frame structures [44], and to investigate the acoustic performance of a periodically voided viscoelastic medium [45] and locally resonant coated plates and shells designed for underwater noise control [46]. Inerter-based chains, with and without local resonators and in the presence of uncertainties, have been investigated by Chatterjee et al. [47] using Monte Carlo (MC) simulations and machine learning. Additionally, Santoro et al. [48] proposed a computational framework to investigate the frequency response of locally resonant metamaterial structures under uncertainty affecting the parameters of resonators. Singh et al. [49] presented a

discussion on the implementation of stochastic modeling for Bloch-Floquet analysis of one- and two-dimensional periodic structures comprising uncertain Young's modulus and density. Longitudinal and flexural wavenumbers were found to be affected by the considered stochastic parameters. Ma and Wang [50] investigated the bandgap characteristics of two-dimensional PCs under material uncertainty and demonstrated that such uncertainties have a significant impact on the final unit cell layout obtained from topology optimization.

In the context of probabilistic approaches, random variables and random fields (or random processes) are used to represent uncertainties in mechanical systems. Specifically, random fields are used to represent space-dependent randomnesses obeying prescribed distribution functions, which requires discretization schemes to render computations amenable. The Karhunen-Loève (KL) expansion is recognized as one of the most effective of such techniques, being optimal in the L^2 sense [51, 52], and has been used to model spatially varying uncertainties in various dynamic problems, ranging from material and geometrical spatially correlated randomness [53] to random dynamic loading [54]. Its foundations are presented in [55], which lay the groundwork for its widespread application and theoretical understanding. Other approaches for modeling random fields are also available in the literature, such as Polynomial Chaos expansion [56], Covariance Matrix Decomposition [57], and Proper Orthogonal Decomposition [58].

Hemanth et al. [59] proposed the finite element matrix formulation of a periodic dielectric structure using stochastic spectral methods with uncertainties in material properties and dimensions. The input random variables were discretized using the KL expansion, and the solution was represented by employing Polynomial Chaos expansion. Mukhopadhyay et al. [60] investigated the stochastic effects of viscoelasticity on spatially correlated quasi-periodic hexagonal lattices. Structural and material irregularities were represented as random fields, discretized using the KL expansion, assuming a Gaussian distribution for the input random variables. Borges et al. [61] evaluated the influence of random temperature distributions on the natural frequencies of thin rectangular plates, where the KL expansion was used to discretize the random temperature fluctuation field. The dispersion of natural frequencies was related to fluctuations of the temperature field. In addition, since thermal stresses can induce buckling, the reliability considering this type of structural failure was estimated.

In fact, reliability analysis is a topic that frequently arises when perform-

ing uncertainty quantification in structural systems. It serves as a measure of the probability of a structure meeting specified criteria established during the design phase, such as safety margins, performance targets, durability and serviceability limits [62, 63]. In despite of the abundance of research papers on reliability analysis of structural systems, few works have been conducted regarding reliability assessment of periodic structures taking into account uncertainties. Among them, it is worth mentioning the recent work of Zhang et al. [64], where a virtual model-aided framework was developed to estimate the structural reliability for elastic metamaterials considering material and geometrical uncertainties separately and simultaneously.

In the context delineated above, the present paper is intended to provide contributions to the characterization of the dynamic behavior of beam-like periodic structures in the simultaneous presence of two relevant types of uncertainties, namely: a) those induced by environmental effects (i.e., temperature), which are considered to affect the material properties and also induce stress-stiffnening effects; and b) those affecting the BCs. The main objective is to investigate the combined influence of such uncertainties, which are likely to be found in practical applications, on the central frequency and bandwidth of attenuation bands of periodic beams. It is then expected that, by accounting for those uncertainties, numerical predictions can get closer to realistic scenarios.

Figure 1 illustrates the problem in consideration, consisting of a periodic beam made of a single linear, homogeneous, isotropic material. Each of the nominally identical unit cells comprises two successive segments with different cross-section dimensions. The analyses are focused on the bending motion of the beam in the y-direction. The BCs at each extremity are represented by translational and rotational springs, the stiffness coefficients of which are modeled as Gaussian random variables and denoted as $k_x^{\mathrm{L}}(\theta)$, $k_y^{\mathrm{L}}(\theta)$, $k_\beta^{\mathrm{L}}(\theta)$, $k_x^{\mathrm{R}}(\theta)$, $k_y^{\mathrm{R}}(\theta)$, $k_\beta^{\mathrm{R}}(\theta)$, with θ being used to indicate random quantities belonging to sample spaces of the associated probability spaces. Also indicated in Fig. 1 is a temperature random field, denoted as $T(x, \theta)$, which varies along the span-wise direction of the beam.

The temperature fluctuations along the length of the beam are modeled as a unidimensional Gaussian random field, which is discretized using the KL expansion. Structural modeling is carried out based on the Stochastic Finite Element Method (SFEM) for the computation of transmissibility functions. Uncertainty quantification is performed based on MC simulations, consid-

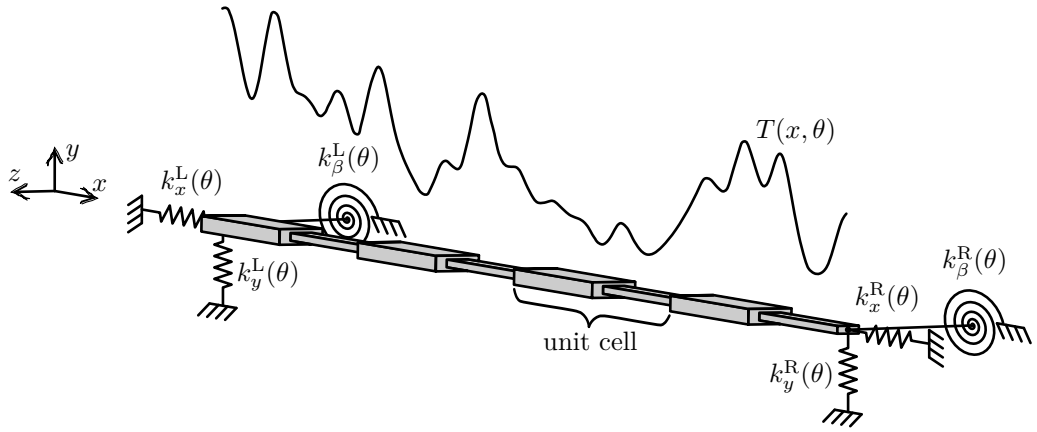


Figure 1: Non-ideally supported periodic beam subjected to a temperature random field.

ering, as output variables, the central frequency and breadth of a chosen attenuation band. In the numerical simulations, different dispersion levels of the random variables are considered, as well as distinct correlation lengths assumed for the temperature random field. Reliability analysis is also performed to assess compliance with design requirements.

In the remainder of this work, the underlying theoretical aspects relevant to the research are initially summarized. First, the modeling of deterministic and stochastic beams, accounting for non-ideal BCs and stress-stiffening induced by thermal effects, is discussed in Section 2. Next, in Section 3, the scenarios defined for numerical simulations are introduced, and the corresponding results are presented and analyzed. Finally, conclusions of the investigation are presented in Section 4.

2. Modeling

The following subsections discuss the deterministic and stochastic modeling of finite and infinite periodic beams, accounting for non-ideal BCs and stress-stiffening induced by thermal effects. While one uses the traditional and stochastic finite element methods for such purpose, other strategies have been proposed to model periodic structures, such as homogenization-based and wave-based techniques [65, 66], and to perform uncertainty quantification, e.g., stochastic perturbation and spectral techniques [67–69], which could be resorted to, alternatively. In this respect, the choice of methodology has been driven mostly by the widespread use of the stochastic finite element

method.

2.1. Deterministic modeling of periodic beams

To model the system shown in Fig. 1, one makes use of two-node, one-dimensional beam finite elements, obeying the Euler-Bernoulli theory, considering a linear, elastic, isotropic material. It is assumed that the beam lies on the x-y plane, its axis initially coincident with the x direction. To describe planar motion, each node has transverse displacement (along y) and in-plane rotation (around z) as degrees-of-freedom (DoFs). The equations of motion for such an element, accounting for stress-stiffening due to axial load, and neglecting damping mechanisms, can be written as [70]:

$$\mathbf{M}^{(\mathrm{e})}\ddot{\mathbf{q}}^{(\mathrm{e})}(t) + \left(\mathbf{K}_{\mathrm{E}}^{(\mathrm{e})} + \mathbf{K}_{\mathrm{G}}^{(\mathrm{e})}\right)\mathbf{q}^{(\mathrm{e})}(t) = \mathbf{f}^{(\mathrm{e})}(t), \tag{1}$$

with $\mathbf{q}^{(\mathrm{e})}(t)$ and $\mathbf{f}^{(\mathrm{e})}(t)$ representing time-dependent vectors of DoFs and loads, respectively; and $\mathbf{M}^{(\mathrm{e})}$, $\mathbf{K}_{\mathrm{E}}^{(\mathrm{e})}$, and $\mathbf{K}_{\mathrm{G}}^{(\mathrm{e})}$ indicating the mass, elastic stiffness, and geometric stiffness matrices, respectively given by:

$$\mathbf{M}^{(\mathrm{e})} = \int_0^{l^{(\mathrm{e})}} \rho^{(\mathrm{e})}(x) A^{(\mathrm{e})}(x) \mathbf{\Psi}^{\mathrm{T}}(x) \mathbf{\Psi}(x) \mathrm{d}x, \tag{2}$$

$$\mathbf{K}_{\mathrm{E}}^{(\mathrm{e})} = \int_0^{l^{(\mathrm{e})}} E^{(\mathrm{e})}(x) I_z^{(\mathrm{e})}(x) \tfrac{\mathrm{d}^2}{\mathrm{d}x^2}\mathbf{\Psi}^{\mathrm{T}}(x) \tfrac{\mathrm{d}^2}{\mathrm{d}x^2}\mathbf{\Psi}(x) \mathrm{d}x, \tag{3}$$

$$\mathbf{K}_{\mathrm{G}}^{(\mathrm{e})} = N^{(\mathrm{e})} \int_0^{l^{(\mathrm{e})}} \tfrac{\mathrm{d}}{\mathrm{d}x}\mathbf{\Psi}^{\mathrm{T}}(x) \tfrac{\mathrm{d}}{\mathrm{d}x}\mathbf{\Psi}(x) \mathrm{d}x. \tag{4}$$

In these equations, $\mathbf{\Psi}(x)$ collects shape functions, $A^{(\mathrm{e})}(x)$ denotes the beam cross-sectional area, $I_z^{(\mathrm{e})}(x)$ is the second moment of area of the cross section about z, $E^{(\mathrm{e})}(x)$ is the material Young's modulus, $\rho^{(\mathrm{e})}(x)$ its volumetric density, $\alpha^{(\mathrm{e})}(x)$ its coefficient of linear thermal expansion, $l^{(\mathrm{e})}$ is the element length, and $N^{(\mathrm{e})}$ is the axial force resulting from constrained thermal dilatation — cf. Subsection 2.1.1.

By considering load equilibrium and displacement/rotation continuity at nodes shared by neighboring elements, Eq. (1) can be rewritten at the global level as:

$$\mathbf{M}^{(\mathrm{g})}\ddot{\mathbf{q}}^{(\mathrm{g})}(t) + \left(\mathbf{K}_{\mathrm{E}}^{(\mathrm{g})} + \mathbf{K}_{\mathrm{G}}^{(\mathrm{g})}\right)\mathbf{q}^{(\mathrm{g})}(t) = \mathbf{f}^{(\mathrm{g})}(t), \tag{5}$$

whose version in the frequency domain is:

$$\left[-\omega^2\mathbf{M}^{(\mathrm{g})} + \mathbf{K}_{\mathrm{E}}^{(\mathrm{g})} + \mathbf{K}_{\mathrm{G}}^{(\mathrm{g})}\right]\mathbf{Q}^{(\mathrm{g})}(\omega) = \mathbf{F}^{(\mathrm{g})}(\omega), \tag{6}$$

with ω denoting the circular frequency of harmonic excitation.

To account for the fact that the beam's end clamps are non-ideal, as shown in Fig. 1, assuming that it is discretized into p finite elements, resulting in $p+1$ nodes, and $2p+2$ DoFs, the elastic stiffness matrix $\mathbf{K}_{\mathrm{E}}^{(\mathrm{g})}$ must be updated as follows:

$$\tilde{\mathbf{K}}_{\mathrm{E}}^{(\mathrm{g})} = \mathbf{K}_{\mathrm{E}}^{(\mathrm{g})} + k_y^{\mathrm{L}}\mathbf{e}_1\mathbf{e}_1^{\mathrm{T}} + k_\beta^{\mathrm{L}}\mathbf{e}_2\mathbf{e}_2^{\mathrm{T}} + k_y^{\mathrm{R}}\mathbf{e}_{2p+1}\mathbf{e}_{2p+1}^{\mathrm{T}} + k_\beta^{\mathrm{R}}\mathbf{e}_{2p+2}\mathbf{e}_{2p+2}^{\mathrm{T}}, \tag{7}$$

where $\mathbf{e}_i$ denotes a column vector of dimension $2p+2$, whose components are zero, except the i-th, which is 1. It should be mentioned that the longitudinal springs with stiffnesses k_x^{L} and k_x^{R}, oriented in the axial direction of the periodic beam, are accounted for differently, as they are related to the thermally-induced axial loads, to be discussed next.

2.1.1. Axial force induced by elastically constrained thermal dilatation

Figure 2 depicts, on the left, a beam of length l, whose extremities are connected in the axial direction to the ground by springs of stiffness coefficients k_x^{L} and k_x^{R}. It also shows, on the right, the same beam under the action of temperature variations and axial force N developed by the axial springs.

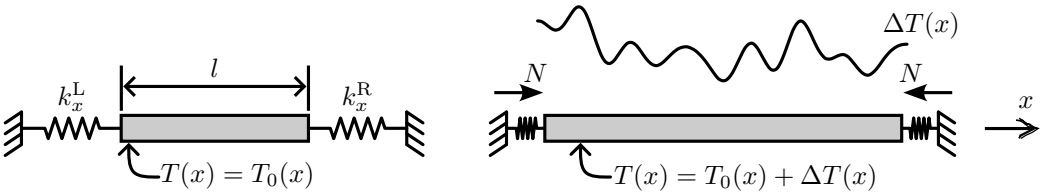


Figure 2: Illustration of a beam in two states: undeformed (left) and elongated under the action of temperature variations and axial forces developed by the axial springs (right).

At a given reference temperature distribution $T(x) = T_0(x)$, the axial springs are undeformed, and do not exert any force on the beam. When the temperature distribution is changed to $T(x) = T_0(x) + \Delta T(x)$, the thermal dilatation becomes partially constrained by the forces N exerted by the springs. Under these conditions, the net elongation of the beam is given by:

$$\Delta l = \Delta l_T + \Delta l_N, \tag{8}$$

where Δl_T is the free thermal elongation and Δl_N is the deformation due to the axial force N, respectively given as [71]:

$$\Delta l_T = \int_0^l \alpha(x)\Delta T(x)\mathrm{d}x, \tag{9}$$

$$\Delta l_N = N\int_0^l \frac{1}{E(x)A(x)}\mathrm{d}x. \tag{10}$$

Considering the axial springs, the following relation holds:

$$\Delta l = -\left(\frac{N}{k_x^{\mathrm{L}}} + \frac{N}{k_x^{\mathrm{R}}}\right). \tag{11}$$

Therefore, the axial force exerted by the springs is:

$$N = -\frac{\displaystyle\int_0^l \alpha(x)\Delta T(x)\mathrm{d}x}{\dfrac{1}{k_x^{\mathrm{L}}} + \dfrac{1}{k_x^{\mathrm{R}}} + \displaystyle\int_0^l \frac{1}{E(x)A(x)}\mathrm{d}x}. \tag{12}$$

According to Eq. (12), the axial force can be interpreted as the one applied to a mechanical system formed by the beam and two springs connected in series, provoking an elongation given by the increment of the thermal dilatation of the beam associated to $\Delta T(x)$. When $k_x^{\mathrm{L}} = k_x^{\mathrm{R}} \to \infty$, the beam experiences no longitudinal elongation, resulting in an ideally clamped-clamped condition. In case $\Delta T(x)$ and $\alpha(x)$ are such that the integral in the numerator of Eq. (12) vanishes, the axial force will be null. This same condition occurs when at least one of k_x^{L} or k_x^{R} is null, meaning that the axial displacement of the corresponding end of the beam is not restrained. In addition, in the absence of other longitudinal axial loads, N is constant along the beam. Hence, $N^{(\mathrm{e})}$ in Eq. (4) shall be computed according to Eq. (12) for each and every finite element of the periodic beam.

2.2. Stochastic modeling of periodic beams with non-ideal boundary conditions and random temperature fluctuations

The temperature random field in Fig. 1 is described using a KL expansion. In this case, $T(x,\theta)$ is represented as the spatially dependent mean temperature field plus a term accounting for fluctuations described by a stationary

one-dimensional Gaussian random field [55]:

$$T(x,\theta) = \bar{T}(x) + \sum_{i=1}^{K} \sqrt{\lambda_i}\xi_i(\theta) f_i(x), \tag{13}$$

where K is the number of terms used in the KL expansion, $\xi_i(\theta)$ represents a set of statistically independent Gaussian random variables with zero mean and specified standard deviation, and λ_i and $f_i(x)$ are the solutions of an integral eigenproblem of the type:

$$\int_D C(x_1,x_2) f_i(x_2) \mathrm{d}x_2 = \lambda_i f_i(x_1), \qquad i = 1,\ldots,K, \tag{14}$$

being $C(x_1,x_2)$ the covariance function assigned to the random field.

Whilst $C(x_1,x_2)$ could be determined from experimental data, via stochastic identification procedures [72–74], here, given that experimental identification is out of scope, one adopts an exponential covariance function, defined on the domain $-l/2 \leqslant x_1, x_2 \leqslant l/2$, such that Eq. (14) becomes:

$$\int_{-l/2}^{l/2} e^{-\frac{|x_1-x_2|}{b}} f_i(x_2) \mathrm{d}x_2 = \lambda_i f_i(x_1), \qquad i = 1,\ldots,K, \tag{15}$$

where b is the correlation length. An important advantage of this choice is that the eigenproblem posed in Eq. (15) has closed-form solution [55].

It should be clarified that the considered random field is fully characterized by its correlation length b and the standard deviation assigned to $\xi_i(\theta)$. In practice, when experimental data are not available, these parameters are frequently set based on expert judgment or by using a broad range of assumed values to cover scenarios as widely as possible [72, 73, 75]. Further details on the selection of these parameters can be found in Subsection 3.1.

The dependence of the Young's modulus on temperature is assumed to be linear, and given by the following relation:

$$E^{(\mathrm{e})}(x,\theta) = mT(x,\theta) + h, \tag{16}$$

where m and h are determined based on experimental data. In contrast, the coefficient of linear thermal expansion and density are assumed to be unaffected by temperature. Although the formulation developed here can accommodate variations in all material properties, this study focus on investigating a beam made of aluminum 6061-T6, a material largely used in

aeronautical structures [76–78], for which the adopted assumptions are well justified [79–81].

Therefore, accounting for Eqs. (13) and (16), the following stochastic version of Eq. (3) is obtained:

$$\mathbf{K}_{\mathrm{E}}^{(\mathrm{e})}(\theta) = \bar{\mathbf{K}}_{\mathrm{E}}^{(\mathrm{e})} + m\sum_{i=1}^{K}\sqrt{\lambda_i}\xi_i(\theta)\int_0^{l^{(\mathrm{e})}} I_z^{(\mathrm{e})}(x) f_i(x+\widetilde{x}_{\mathrm{L}}^{(\mathrm{e})})\tfrac{\mathrm{d}^2}{\mathrm{d}x^2}\boldsymbol{\Psi}^{\mathrm{T}}(x)\tfrac{\mathrm{d}^2}{\mathrm{d}x^2}\boldsymbol{\Psi}(x)\mathrm{d}x, \quad (17)$$

where:

$$\bar{\mathbf{K}}_{\mathrm{E}}^{(\mathrm{e})} = \int_0^{l^{(\mathrm{e})}} \left(m\bar{T}(x)+h\right) I_z^{(\mathrm{e})}(x)\tfrac{\mathrm{d}^2}{\mathrm{d}x^2}\boldsymbol{\Psi}^{\mathrm{T}}(x)\tfrac{\mathrm{d}^2}{\mathrm{d}x^2}\boldsymbol{\Psi}(x)\mathrm{d}x, \quad (18)$$

and $\widetilde{x}_{\mathrm{L}}^{(\mathrm{e})}$ denotes the coordinate $\widetilde{x}$ of the left node of the referred finite element, which is used to relate the global coordinate $\widetilde{x}$ of the KL expansion to the local coordinate system of a finite element, for which $0 \leqslant x \leqslant l^{(\mathrm{e})}$.

As a result of the temperature random field, the force induced by thermal effects (Eq. (12)), which is also affected by the randomness of BCs, is updated to account for both influences simultaneously, as follows:

$$N(\theta) = -\frac{\displaystyle\int_0^{l}\alpha(x)(T(x,\theta)-T_0(x))\mathrm{d}x}{\dfrac{1}{k_x^{\mathrm{L}}(\theta)}+\dfrac{1}{k_x^{\mathrm{R}}(\theta)}+\displaystyle\int_0^{l}\frac{1}{E(x,\theta)A(x)}\mathrm{d}x}. \quad (19)$$

Assuming that $\alpha(x)$ and $A(x)$ are constant within each finite element and $\bar{T}(x)$ and $T_0(x)$ constant along the span of the beam (i.e., $\bar{T}(x)=\bar{T}$ and $T_0(x)=T_0$), Eq. (19) is rewritten as follows:

$$N(\theta) = -\frac{\left(\bar{T}-T_0\right)\displaystyle\sum_{\mathrm{e}=1}^{N_e}\alpha^{(\mathrm{e})}l^{(\mathrm{e})} + \sum_{\mathrm{e}=1}^{N_e}\alpha^{(\mathrm{e})}\sum_{i=1}^{K}\sqrt{\lambda_i}\xi_i(\theta)\displaystyle\int_0^{l^{(\mathrm{e})}} f_i(x+\widetilde{x}_{\mathrm{L}}^{(\mathrm{e})})\mathrm{d}x}{\dfrac{1}{k_x^{\mathrm{L}}(\theta)}+\dfrac{1}{k_x^{\mathrm{R}}(\theta)}+\displaystyle\sum_{\mathrm{e}=1}^{N_e}\frac{1}{A^{(\mathrm{e})}}\int_0^{l^{(e)}}\frac{1}{\gamma(x,\theta)}\mathrm{d}x}, \quad (20)$$

where N_e is the total number of finite elements and:

$$\gamma(x,\theta) = m\left(\bar{T}+\sum_{i=1}^{K}\sqrt{\lambda_i}\xi_i(\theta)f_i(x+\widetilde{x}_{\mathrm{L}}^{(\mathrm{e})})\right)+h. \quad (21)$$

Therefore, the stochastic counterpart of Eq. (4) is given by:

$$\mathbf{K}_{\mathrm{G}}^{(\mathrm{e})}(\theta) = N(\theta) \int_0^{l^{(\mathrm{e})}} \tfrac{\mathrm{d}}{\mathrm{d}x}\boldsymbol{\Psi}^{\mathrm{T}}(x)\tfrac{\mathrm{d}}{\mathrm{d}x}\boldsymbol{\Psi}(x)\mathrm{d}x. \tag{22}$$

Based on Eqs. (17) and (22), the stochastic version of Eq. (6) can be written as:

$$\left[-\omega^2\mathbf{M}^{(\mathrm{g})} + \mathbf{K}_{\mathrm{E}}^{(\mathrm{g})}(\theta) + \mathbf{K}_{\mathrm{G}}^{(\mathrm{g})}(\theta)\right]\mathbf{Q}^{(\mathrm{g})}(\omega,\theta) = \mathbf{F}^{(\mathrm{g})}(\omega). \tag{23}$$

To account for the influence of transverse and rotational springs related to BCs on $\mathbf{K}_{\mathrm{E}}^{(\mathrm{g})}(\theta)$, Eq. (7) is updated to:

$$\begin{aligned}\tilde{\mathbf{K}}_{\mathrm{E}}^{(\mathrm{g})}(\theta) &= \mathbf{K}_{\mathrm{E}}^{(\mathrm{g})}(\theta) \\ &\quad + k_y^{\mathrm{L}}(\theta)\mathbf{e}_1\mathbf{e}_1^{\mathrm{T}} + k_\beta^{\mathrm{L}}(\theta)\mathbf{e}_2\mathbf{e}_2^{\mathrm{T}} + k_y^{\mathrm{R}}(\theta)\mathbf{e}_{2p+1}\mathbf{e}_{2p+1}^{\mathrm{T}} + k_\beta^{\mathrm{R}}(\theta)\mathbf{e}_{2p+2}\mathbf{e}_{2p+2}^{\mathrm{T}}.\end{aligned} \tag{24}$$

In summary, the stochastic model comprises six continuous random variables representing the springs introduced to account for non-ideal BCs, along with a random field representing temperature fluctuations. This latter is discretized using K terms in its KL expansion, resulting in a total number of $K+6$ random variables for the stochastic model.

2.3. Dynamic behavior of infinite and finite periodic beams

Dispersion diagrams characterize free wave propagation in infinite media. For periodic structures, they can be obtained from the finite element model of a single unit cell, accounting for the Bloch-Floquet theorem. In this setting, it is possible to derive the standard eigenproblem [82, 83]:

$$\left(\mathbf{S} - \mu_j\mathbf{I}\right)\boldsymbol{\chi}_j = \mathbf{0}, \qquad j \in \{1,2\}, \tag{25}$$

where μ_j and $\boldsymbol{\chi}_j$ represent the Bloch propagation constants and wave mode shapes, respectively, and $\mathbf{S}$ is the unit cell transfer matrix. Wavenumbers can be obtained as $k_j = (\ln\mu_j)/(-\mathrm{i}\Delta)$, where Δ is the unit cell length along the direction of wave propagation and $\mathrm{i} = \sqrt{-1}$. Purely real and purely imaginary wavenumbers indicate propagating and evanescent (spatially attenuated) waves, respectively, whereas complex wavenumbers are related to decaying, oscillatory waves [84].

On the other hand, the steady state dynamic behavior of finite periodic structures can be characterized by means of frequency response functions. In

particular, transmissibilities ($\mathrm{T}_{ij}(\omega)$) are often used to quantify how vibrations are transmitted through a system, measuring the attenuation characteristics between DoFs i and j. They might be obtained through [85]:

$$\mathrm{T}_{ij}(\omega) = \frac{H_{ij}(\omega)}{H_{jj}(\omega)}, \tag{26}$$

where $H_{ij}(\omega)$ and $H_{jj}(\omega)$ are transfer and driving receptances, respectively, which can be efficiently calculated using mode superposition methods [86].

2.4. Sensitivity analysis

The assessment of the relative contributions of individual random variables to the variability of structural responses is of utmost importance when performing uncertainty quantification. Among other utilities, it provides guidance for selecting the most influential stochastic variables, enabling more efficient modeling with reduced computational effort. A variety of the so-called *sensitivity analysis techniques* have been developed and are richly reported in the literature [87–92]. In [93], authors advocated for sensitivity analysis to become an independent discipline, while also reviewing the various methodologies adequate to perform such task. Among them, a frequently used hybrid local-global sensitivity approach is based on the sigma-normalized relations, i.e., derivatives normalized by the input and output standard deviations [32]. This method focuses on the response fluctuations when the input random variables are perturbed individually about their nominal mean values μ_{Θ_i}. Therefore, the effect of each random variable Θ_i on the variation of a target response g can be computed using the sigma-normalized relation $S^{\sigma}_{\Theta_i}$, as follows:

$$S^{\sigma}_{\Theta_i} = \frac{\partial g(\mu_{\Theta_i})}{\partial \Theta_i} \frac{\sigma_{\Theta_i}}{\sigma_g}, \tag{27}$$

where σ_{Θ_i} and σ_g are the standard deviations of Θ_i and g, respectively. Larger values of $S^{\sigma}_{\Theta_i}$ indicate high degree of sensitivity of g with respect to Θ_i.

The derivatives involving Eq. (27) can be computed analytically, when $g(\mu_{\Theta_i})$ is known explicitly, or using finite differences. The sum of the squares of $S^{\sigma}_{\Theta_i}$ is one, enabling to easily quantify the relative contributions of each random variable on the variation of a target response, i.e. [94]:

$$\sum_{i=1}^{N_\theta} \left(S^{\sigma}_{\Theta_i}\right)^2 = \sum_{i=1}^{N_\theta} \left(\frac{\partial g(\mu_{\Theta_i})}{\partial \Theta_i} \frac{\sigma_{\Theta_i}}{\sigma_g} \right)^2 = 1, \tag{28}$$

where N_θ is the total number of random variables considered in the stochastic model and:

$$\sigma_g = \sqrt{\sum_{i=1}^{N_\theta} \left(\frac{\partial g(\mu_{\Theta_i})}{\partial \Theta_i} \sigma_{\Theta_i} \right)^2}. \tag{29}$$

2.5. Additional remarks

The stochastic modeling of periodic beams with non-ideal BCs and random temperature fluctuations has been addressed in the previous subsections. To further clarify the proposed methodology, Fig. 3 presents a flowchart which illustrates the various steps followed to perform simulations.

As can be seen from the referred flowchart, analyses start with the definition of the problem parameters, including the geometry, material properties, and mean and reference temperature fields. Next, samples are generated for the random variables related to the BCs and temperature fluctuations. In this regard, one emphasizes that one assumes the random variables related to BCs to be statistically independent from those related to the KL expansion of the temperature fluctuations field. For simplicity, one also assumes the random variables related to the uncertain BCs to be statistically independent with respect to each other, as well. Taking this into account, samples are generated in accordance with the underlying, adopted probability distributions, respecting the mentioned independences or eventual correlations. In Fig. 3, one also highlights steps associated with the KL expansion of the temperature fluctuations random field, comprising the computation of λ_i and f_i, as well as $T(x, \theta)$. The stochastic elementary stiffness finite element matrices are computed in accordance with the SFEM, together with the deterministic mass matrix, allowing the assembly of the uncertain dynamic stiffness matrix appearing in Eq. (23). Boundary conditions are afterward enforced by proper modification of $\mathbf{K}_{\mathrm{E}}^{(\mathrm{g})}(\theta)$ ($\mathbf{K}_{\mathrm{E}}^{(\mathrm{g})}(\theta) \rightarrow \tilde{\mathbf{K}}_{\mathrm{E}}^{(\mathrm{g})}(\theta)$). This is followed by the computation of the transmissibility curve for the sample being studied, which concludes what one has identified as MC simulations in the flowchart. Next, the computation of bandgap features is conducted, which is a step one clarifies in Section 3. Finally, uncertainty quantification, sensitivity and reliability analyses for the periodic beam with non-ideal BCs and random temperature fluctuations are performed.

At this stage, it is worth making the following comments regarding some of the choices and simplifications adopted in the proposed methodology.

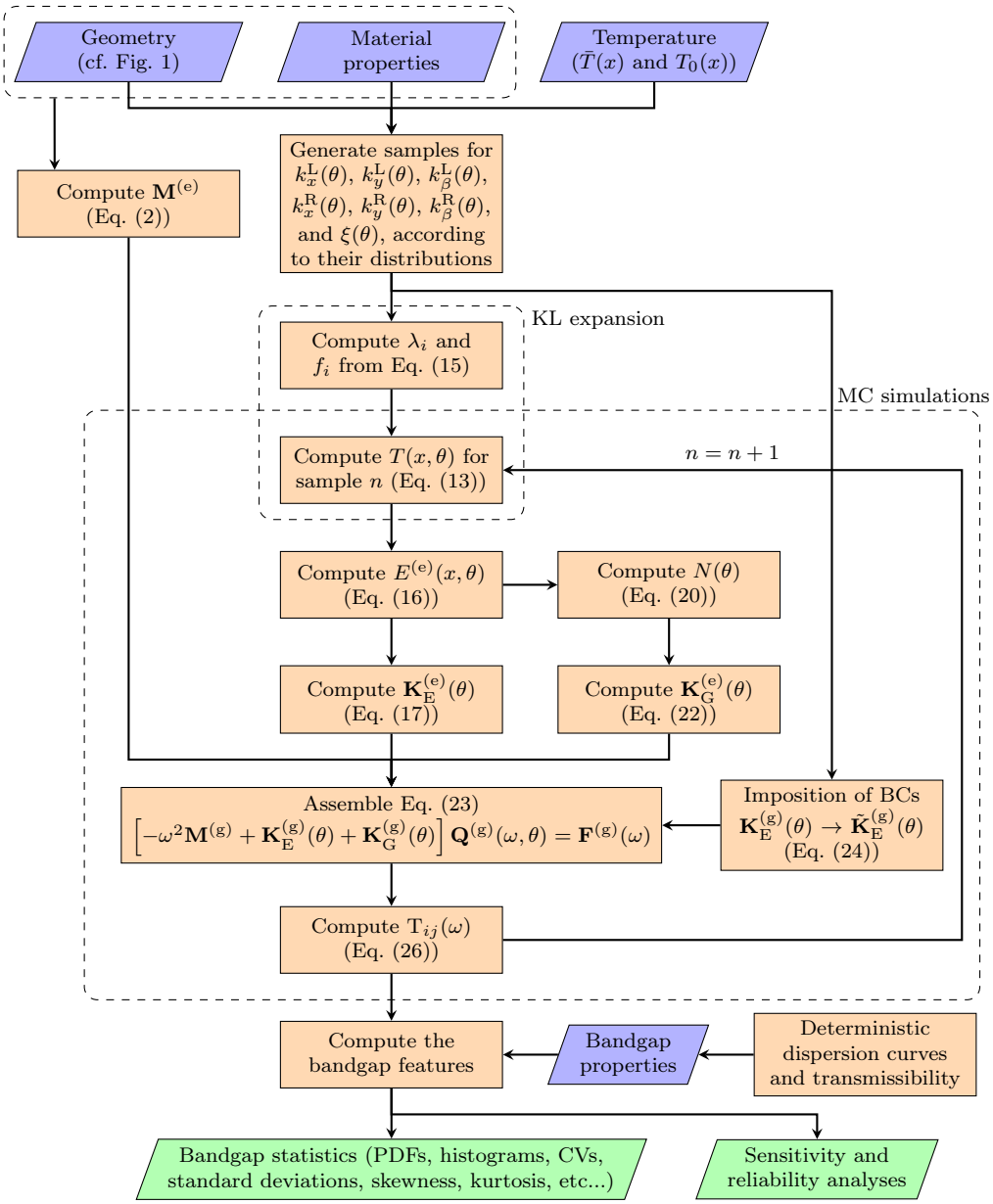


Figure 3: Flowchart illustrating the various steps for the stochastic modeling of periodic beams with non-ideal BCs and random temperature fluctuations.

First, one should recognize that probability distributions have been assumed to be previously known for the considered uncertain quantities, which might not be the case in practical situations. In addition, in some circumstances one would need to consider the so-called reducible or epistemic uncertainties, engendered by the lack of knowledge or information in any phase of the modeling process, including the lack of previous knowledge about the probability distributions. To handle, at least partially, the lack of knowledge, one could suitably resort to the principle of maximum entropy, for example [33, 52], which states that the probability density function (PDF) with the highest information entropy is the best PDF among all PDFs that satisfy a set of given constraints. Additionally, if data would become available, Bayesian inference, for example, could be resorted to, for updating a prior distribution to more accurately describe the underlying random quantity [74].

Second, besides admitting probability distributions to be previously known, one also assumes them to be Gaussian. In the case of the temperature fluctuations, its is fair to consider that its variability would result from the combination of various random influences, affecting heat transfer mechanisms at atomic or molecular levels — such that their combined effect would result Gaussian, by the central limit theorem. On the other hand, the fact that the stiffness coefficients of the springs representing non-ideal boundary conditions must take strictly non-negative values is, indeed, incompatible with Gaussian distributions ascribed to them. However, the mean values and standard deviations ascribed to them makes the occurrence of negative values to be events of very low probability, which have not been observed in the simulations performed.

In summary, the option for Gaussian distributions is justified by the more straightforward theoretical and numerical procedures required, with no loss in the achievement of the objectives established for the present investigation.

It is also worth mentioning that, despite the arguments above, several works have employed non-Gaussian random fields, particularly characterized by marginal gamma distributions, or sometimes marginal log-normal distributions, for modeling spatially varying quantities [95–99]. The random stiffness of springs have also been modeled following uniform, exponential, gamma, or log-normal probability distributions, depending on available information, in accordance with the principle of maximum entropy [33, 52].

In this sense, it is important to mention that the formulation developed here can be suitably extended to accommodate covariance functions other than the exponential one used here for the random field representing tem-

perature fluctuations. Furthermore, the uncertain parameters and field could be modeled using non-Gaussian marginal distributions, if needed or desired. Certainly, additional difficulties would arise, as reported in the literature on the generation/sampling of non-Gaussian random fields [100, 101].

Third, it is worth remarking that, as the random temperature fluctuations field has been modeled assuming it to be a stationary Gaussian, cf. Eq. (13), the beam's Young's modulus also behaves as a stationary Gaussian random field, as a consequence of Eq. (16). The same modeling approach has been adopted by Parviz and colleagues, where the free vibration [102, 103] and thermal stability [104] of laminated composite plates with spatially-dependent temperature material were addressed. Analogously to what has been proposed in the current work, Parviz and collaborators assumed a linear dependency between the Young's modulus and temperature, employing the KL expansion to discretize the temperature random field.

3. Results and discussions

The subsections below present several results from numerical simulations and related discussions. First, the problem definition is outlined in Subsection 3.1. Then, in Subsection 3.2, before proceeding with stochastic dynamic analyses of the periodic beam under uncertain BCs and temperature fluctuations, deterministic analyses are presented. To enable a more comprehensive characterization of the influences exerted by the two sources of uncertainty, in Subsection 3.3 the influence of randomness in BCs is evaluated, admitting the temperature field as deterministic. Next, in Subsection 3.4, environmental uncertainties resulting from the temperature random field are considered, while the stiffness coefficients related to the non-ideal BCs take their deterministic mean values. Finally, in Subsection 3.5, the combined effects of uncertainties from BCs and temperature fluctuations on the dynamics of the nominally periodic beam are investigated. Reliability and sensitivity analyses are provided to assess the impact of these uncertainties on the overall dynamic behavior of the system.

3.1. Problem statement

For the numerical computations that follow, the system depicted in Fig. 1 is considered. It consists of an aluminum beam with a total length of 1 m, with four identical unit cells, each one composed of two segments. Each segment is 125 mm long ($\Delta = 250$ mm), with the left-hand and right-hand

segments having rectangular cross-sections measuring $30\,\mathrm{mm} \times 10\,\mathrm{mm}$ and $15\,\mathrm{mm} \times 5\,\mathrm{mm}$, respectively.

The reference temperature used to compute the thermally-induced axial force N, indicated in Fig. 2, is considered to be uniform with value $T_0(x) = T_0 = 25°\mathrm{C}$. Aiming at investigating a situation commonly found in aeronautical engineering, where parts are manufactured at room temperature but may operate at very low temperatures at cruising altitudes, it is assumed that the mean temperature of the random field, introduced in Eq. (13), is also uniform and equal to $\bar{T}(x) = \bar{T} = -30°\mathrm{C}$, which closely approximates real situations [105–108].

Regarding the dependency of material parameters on temperature, ref. [81] states that a fourth-order polynomial can represent adequately the variation of the Young's modulus in the range 2 K–295 K for the aluminum alloy 6061-T6. However, the linear relationship assumed in Eq. (16) reasonably predicts this dependency in a narrower temperature range, which is of interest in this work. Thus the fourth-order relationship provided in [81] is linearized by using Taylor series expansion about the mean temperature of the random field, which gives $E = mT + h$, with $m = -33.95\,\mathrm{MPa\,K^{-1}}$ and $h = 80.37\,\mathrm{GPa}$. Furthermore, the mass density and coefficient of linear thermal expansion are assumed to be unaffected by temperature variations, as discussed in Subsection 2.2, so that $\rho = 2700\,\mathrm{kg\,m^{-3}}$ and $\alpha = 2.12 \times 10^{-5}°\mathrm{C^{-1}}$ are adopted.

The mean values of the Gaussian random variables associated with the stiffness coefficients related to the non-ideal BCs are set as $\mu_{k_x^{\mathrm{L}}} = \mu_{k_x^{\mathrm{R}}} = 0.2\,\mathrm{GN\,m^{-1}}$, $\mu_{k_y^{\mathrm{L}}} = \mu_{k_y^{\mathrm{R}}} = 0.1\,\mathrm{GN\,m^{-1}}$, and $\mu_{k_\beta^{\mathrm{L}}} = \mu_{k_\beta^{\mathrm{R}}} = 1\,\mathrm{MN\,m\,rad^{-1}}$. To justify these choices, it is important to consider that the dynamic behavior of the beam is strongly influenced by the values of these stiffness parameters. In fact, these values can represent any situation ranging from ideally free to ideally clamped BCs, when they are chosen sufficiently small or sufficiently large, respectively [109]. As the interest here is to consider deviations from the ideally clamped condition, prior numerical simulations were performed to determine mean values of the stiffness parameters ensuring this situation, based on the value observed for the highest natural frequency of the beam in the frequency band of interest.

For the analyses presented next, the correlation length of the exponential covariance function appearing in Eq. (15) was admitted to take values in a broad range: $b = 0.05\Delta$, Δ, 2Δ, and 26Δ. Preliminary analyses were

conducted to determine relevant simulation parameters. Firstly, for the KL expansions, values of $K = 340$, 18, 10, and 2 were chosen for $b = 0.05\Delta$, Δ, 2Δ, and 26Δ, respectively. This selection followed the procedure outlined in ref. [32], which suggests that the sum of the truncated eigenvalues should be sufficiently small compared to the sum of the K retained ones. Therefore, convergence for the KL expansion was considered achieved when the ratio of the sum of the truncated eigenvalues to the sum of the retained ones was below 5%.

Moreover, the periodic beam was discretized employing $N_e = 80$ finite elements, which largely ensures mesh convergence of the finite element model within the frequency range of analysis, set from 0 Hz to 2000 Hz (with Δf = 1 Hz). For the computation of frequency response functions using the modal superposition method, retaining the modes corresponding to natural frequencies up to ten times the upper limit of the frequency band of interest was found to be sufficient to guarantee satisfactory accuracy.

Additionally, due to the relatively high computational cost required to perform the multiple integrations appearing in the denominator of Eq. (20), a numerical integration scheme employing global adaptive quadrature with an absolute error tolerance of 1×10^{-10} was employed (MATLAB® command `integral`).

For uncertainty propagation, 10000 samples were found sufficient to ensure convergence of MC simulations. Regarding the sensitivity analysis discussed in Subsection 2.4, care was exercised in the choice of the increments used for the computation of finite-difference approximations to the derivatives appearing in Eq. (27), which were established by means of convergence check for a target response, for each random variable.

After performing convergence analyses, dispersion curves enabling to predict bandgaps for the baseline deterministic system (infinite beam) were obtained. The results from this analysis were then used to characterize attenuation bands for samples of the finite periodic beam in the stochastic analyses. The influence of the standard deviations assigned to the input random variables on the responses, taking into account the aforementioned correlation lengths, was evaluated through different values of coefficients of variation (CVs), defined as the ratio of the standard deviation to the mean, i.e., CV = 1%, 10% and 20%. In addition, it should be reminded that the random variables related to the KL expansion, ξ_i, form a set of independent, zero-mean Gaussian random variables, cf. Subsection 2.2. Their standard deviations have been obtained using the mean temperature of the random field, i.e.,

$\sigma_{\xi_i} = \text{CV} \times \bar{T}$. Analyses were also conducted with the aim of evaluating the influence of each considered correlation length on the dynamics of the periodic beam, while keeping the CV fixed.

Concerning the results reported below, one clarifies the associated simulations have been executed on a DELL XPS 8950 desktop computer equipped with an Intel(R) Core(TM) i7-12700 CPU running at 2.10 GHz and 16.0 GB of RAM. When only the randomnesses in BCs is considered (Subsection 3.3), which involves 6 random variables, the computation of forced responses for a given value of CV and standard deviation took less than half an hour. On the other hand, when the combined randomness in BCs and temperature is considered, along with a shorter correlation length (Subsection 3.5), the simulation time increased to approximately 5 hours, as it involved 346 random variables.

Lastly, it should be clarified that the selection of relevant parameters for the temperature random field, such as the CV and correlation length b, as well as the CV for the uncertain BCs, has been made to cover a range of scenarios as wide as possible.

3.2. Deterministic analyses

By employing the theory reviewed in Subsection 2.3 and the mean values adopted for all random variables and for the temperature random field, wavenumbers were computed for the periodic beam. One highlights that the unit cell mass and stiffness matrices were assembled based on Eqs. (2)–(4), with $N^{(\text{e})}$ computed according to Eq. (12) for the deterministic finite structure composed of 4 unit cells. In addition, the Young's modulus was set as $E = m\bar{T} + h = 72.12\,\text{GPa}$, by relying on the non-stochastic version of Eq. (16). The obtained dispersion relation, depicted in Fig. 4a, shows that the infinite periodic beam possesses two bandgaps in the frequency range of interest, i.e., 336–393 Hz and 945–1534 Hz, indicated by the shaded regions.

By assuming that the transversal DoF of the rightmost free node of the beam is harmonically excited, and the response is calculated for the same DoF of the leftmost free node, as schematically shown in Fig. 4b, the corresponding transmissibility function $\text{T}_{(3,159)}$, computed using Eq. (26), is shown in Fig. 4c. It should be pointed-out that this transmissibility was computed for the beam supported by flexural, torsional and axial springs, to which the respective mean values were assigned, as discussed previously.

As one may notice from Fig. 4c, the bandgaps predicted in the dispersion diagram match the very low-amplitude regions seen in the transmissibility

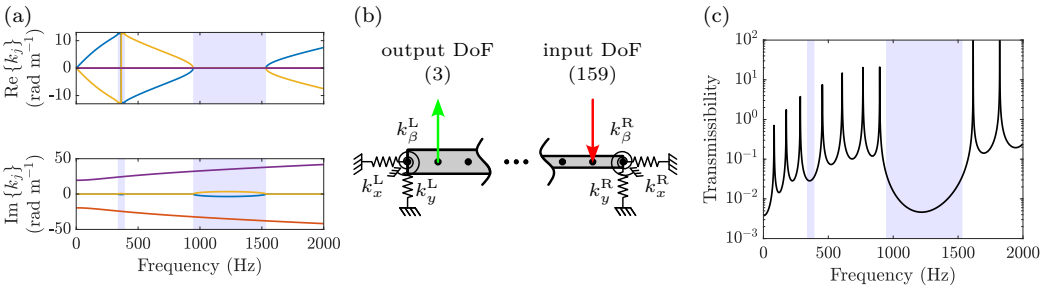


Figure 4: (a) Real and imaginary parts of the dispersion relation for the deterministic periodic beam, with bandgaps highlighted by shaded areas; (b) identification of input and output DoFs used to generate the transmissibility function and (c) amplitudes of the transmissibility function $\mathrm{T}_{(3,159)}$, with the associated attenuation bands highlighted. Mean values were adopted for all random variables and for the temperature random field.

curve. Interestingly, the range of frequencies lower than the first resonance frequency exhibits attenuation levels of the order of those found in the second attenuation zone. This observation was similarly reported in [110], for a periodic rod-type structure, and is attributed to BC effects.

As the second attenuation band is much wider than the first one, which is interesting from the practical point of view, the stochastic analyses carried out in the sequence are exclusively devoted to this wider band, for which the limiting frequencies are $f_{\mathrm{L}} = 945$ Hz and $f_{\mathrm{R}} = 1534$ Hz.

For the purpose of assessing the influence of random quantities, to be conducted next, from the transmissibility curve shown in Fig. 4c, one extracts the amplitudes corresponding to f_{L} and f_{R}, which are $\mathrm{T}_{\mathrm{L}} \approx 0.044$ and $\mathrm{T}_{\mathrm{R}} \approx 0.038$. In addition, one determines the central frequency of the attenuation zone:

$$f_{\mathrm{central}} = \frac{f_{\mathrm{L}} + f_{\mathrm{R}}}{2} = 1239.5\,\mathrm{Hz}, \tag{30}$$

and its bandwidth:

$$f_{\mathrm{width}} = f_{\mathrm{R}} - f_{\mathrm{L}} = 589\,\mathrm{Hz}. \tag{31}$$

3.3. Randomness in boundary conditions

Stochastic simulations were first performed to evaluate the impact of the uncertainties in the BCs on the attenuation zone of interest. The fact that the axial force given by Eq. (19) is dependent on the variability of the axial springs implies that this force is random under deterministic temperature

distribution. Accordingly, Fig. 5 shows PDFs in solid black lines, estimated using Kernel's density estimator, superimposed on histograms, as well as statistics related to $N(\theta)$, for different values of CV ascribed to the input random variables. One clarifies that the standard deviations, skewness, and kurtosis values reported in Fig. 5, and in what follows afterward, were all calculated using unbiased estimators, whose expressions can be consulted in the documentation of the used software [111–113].

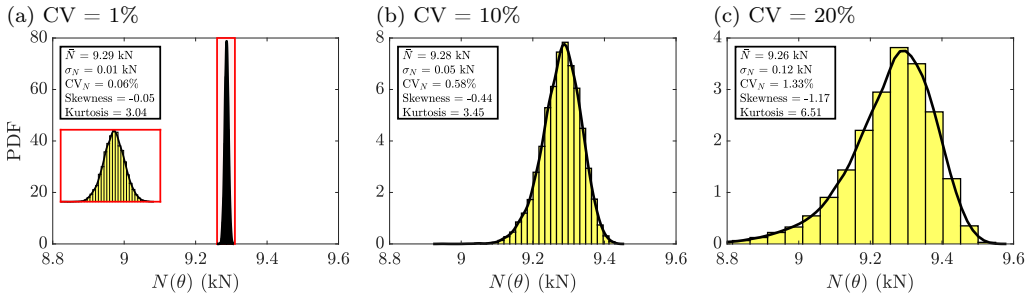


Figure 5: Histograms, PDFs, and statistics related to the stochastic axial force, for different CVs, solely accounting for the randomness of BCs while maintaining the temperature field at the mean value $\bar{T} = -30°\text{C}$.

It can be seen in Fig. 5 that the mean values of the stochastic axial forces are approximately the same for the three cases, i.e., $\approx 9.28\,\text{kN}$, which is close to the value of the axial force obtained for the mean values of the temperature random field and axial stiffness coefficients representing the BCs. In addition, the standard deviation of the axial force, σ_N, exhibits a nonlinear relationship with the CV of the input random variables.

Another observation in Fig. 5 is that, as the CV assigned to the input random variables increases, the skewness values become more negative, revealing that the distributions have a slightly longer tail on the left side of their peak, i.e., they become more asymmetric. It is also apparent from Fig. 5 that all PDFs are steep, as indicated by the kurtosis values, which increase for increasing CV, varying from 3.04 to 6.51.

The increasing asymmetry of the PDFs for increasing CV in Fig. 5 can be physically interpreted considering that the mean values of the spring coefficients were selected to simulate a condition close to the ideally clamped one. Hence, values of k_x^{L}, k_y^{L}, k_β^{L}, k_x^{R}, k_y^{R}, and k_β^{R} higher than their mean values lead asymptotically to this condition, while lower values produce more pronounced approximation to the free-end BC.

Monte Carlo simulations were also performed to characterize the bandgap features of the periodic beam. For each value of CV, transmissibility functions were computed for the input and output locations illustrated in Fig. 4b, using Eq. (26). Figure 6 displays the envelopes of all 10000 samples shaded in gray, along with some arbitrarily selected transmissibility samples. The rectangular regions shaded in purple represent the intersection of the attenuation bands identified for each sample, thus indicating the narrowest attenuation band (NAB) observed across all samples. For each sample, the boundaries of the attenuation band, denoted as $f_{\mathrm{L}}(\theta)$ and $f_{\mathrm{R}}(\theta)$, were determined as the frequencies corresponding to $\mathrm{T_L} \approx 0.044$ and $\mathrm{T_R} \approx 0.038$, obtained previously for the reference deterministic case in Subsection 3.2.

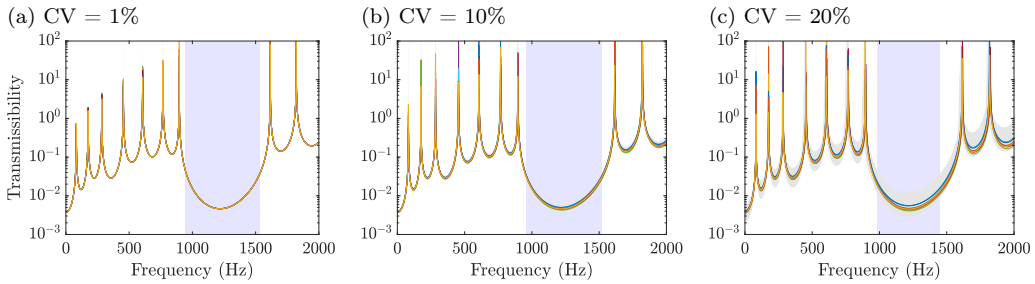


Figure 6: Envelopes of all 10000 samples of transmissibility curves $\mathrm{T}_{(3,159)}$ shaded in gray, and some arbitrarily selected transmissibility samples, solely accounting for the randomness of BCs while maintaining the temperature field with the mean value $\bar{T} = -30°\mathrm{C}$. Shaded purple rectangular regions indicate the intersection of stop bands of all samples.

Figure 6a indicates that, as expected, when the level of dispersion assigned to the random variables related to BCs is low, i.e., CV = 1%, uncertainties affecting the transmissibility curves, and the attenuation bands, as a result, are small within the considered frequency range. On the other hand, considerably narrower attenuation bands are observed for higher CV values, as depicted in Figs. 6b and 6c.

From the stochastic transmissibility curves, characterization of the NABs was conducted by estimating histograms, PDFs and related statistics for the central frequency and bandwidth, computed according to Eqs. (30) and (31). Firstly, Fig. 7 shows PDFs and statistics related to the bandgap central frequency. Similarly to the results presented in Fig. 5, the probability distributions and statistics for lower values of CV resemble those of Gaussian distributions in Figs. 7a and 7b, while the PDF in Fig. 7c shows noticeable deviations from a Gaussian shape (cf. the skewness and kurtosis values). In

all cases, the central frequency of the NAB has approximately the same value, of 1239 Hz, revealing that, on average, dispersion in the input random variables (BCs) mostly affects the bandgap boundaries. Figure 7 also indicates that $\sigma_{f_{\text{central}}}$ exhibits a nonlinear variation for increasing values of CV. This finding is consistent with the result observed previously in Fig. 5, regarding the dispersion of the stochastic axial force σ_N.

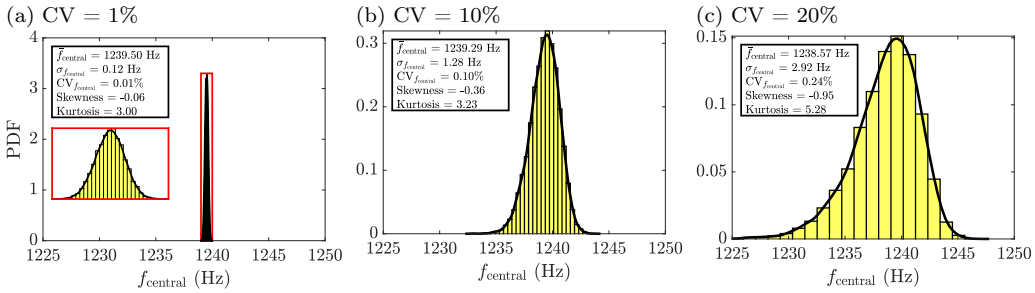


Figure 7: Histograms, PDFs, and statistics of central frequency distributions for different values of CVs, solely accounting for the randomness of BCs while maintaining the temperature field with the mean value $\bar{T} = -30°\text{C}$.

Figure 8 provides histograms, fitted PDFs and statistics for the bandgap width. Overall, the tendencies of the results in Fig. 8 are similar to those in Fig. 7. Therefore, the distributions of the bandgap width for lower CV values resemble a Gaussian distribution, as confirmed by their skewness and kurtosis values close to 0 and 3, respectively. On the other hand, greater levels of variability assigned to the uncertain BCs result in deviations from Gaussian distribution, as depicted in Fig. 8c. It should also be noted from Fig. 8 that $\sigma_{f_{\text{width}}}$ increases in a nonlinear manner as CV grows, behaving similarly to $\sigma_{f_{\text{central}}}$.

3.4. Random temperature field

Based on Eq. (13), 10000 samples of the temperature random field were generated. Figure 9 depicts the envelopes encompassing all the samples (indicated by the shaded areas), and 10 arbitrarily chosen samples, for different combinations of values of the correlation length b and coefficient of variation CV. The interest here is to investigate the influence of these two parameters, which usually must be chosen by the analyst based on the information available.

In Figs. 9a–9d, one can appraise the influence of b, for a fixed CV, while the influence of CV, for a fixed value of b, is assessed in Figs. 9e, 9c, and 9f.

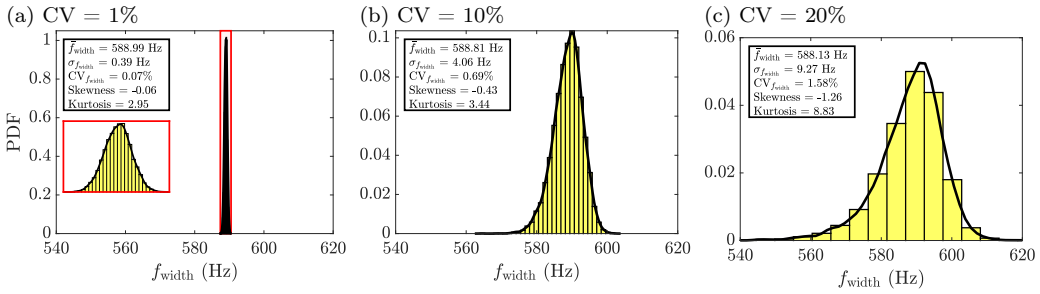


Figure 8: Histograms, PDFs, and statistics of bandwidth distributions for different CVs, solely accounting for the randomness of BCs while maintaining the temperature field with the mean value $\overline{T} = -30°\text{C}$.

Also shown in Fig. 9 are the corresponding means and standard deviations of the random fields, which demonstrate that the MC simulations achieved satisfactory convergence for the stochastic inputs.

As pointed out in [75], Fig. 9a shows that when the correlation length is small, the temperature random field approaches a white-noise type of stochastic process. In addition, under this condition, high spatial frequency components are dominant, thus more terms are needed to properly describe the KL expansion (i.e., 340 eigensolutions, as defined in Subsection 3.1). Conversely, Figs. 9b–9d indicate that, as the correlation length increases, the spatial variation of the random field becomes smoother. For large values of the correlation length ($b = 26\Delta$, for example), the random process tends to become fully correlated. In this latter case, the random field tends to behave as a single, space-independent, random variable (cf. Fig. 9d). Moreover, for large values of b ($b \to \infty$), very low spatial frequency components are dominant and fewer terms are sufficient to represent the temperature random field by KL expansions — only 2 terms. Interestingly, Figs. 9a–9d also indicate that the correlation length has no influence on the dispersion of the temperature random field. Regarding the influence of the CV, Figs. 9e, 9c, and 9f show that, as expected, for a fixed correlation length, the envelope of the random field is amplified when CV increases.

From the samples of the temperature random field, the corresponding values of the axial force have been computed according to Eq. (20), with $k_x^{\text{L}}(\theta) = \mu_{k_x^{\text{L}}}$ and $k_x^{\text{R}}(\theta) = \mu_{k_x^{\text{R}}}$. Figure 10 illustrates the resulting PDFs (in solid black lines) estimated using Kernel's density estimator, superimposed to the corresponding histograms. It is worthy noticing that the axial force also depends on the random field representing the temperature-dependent

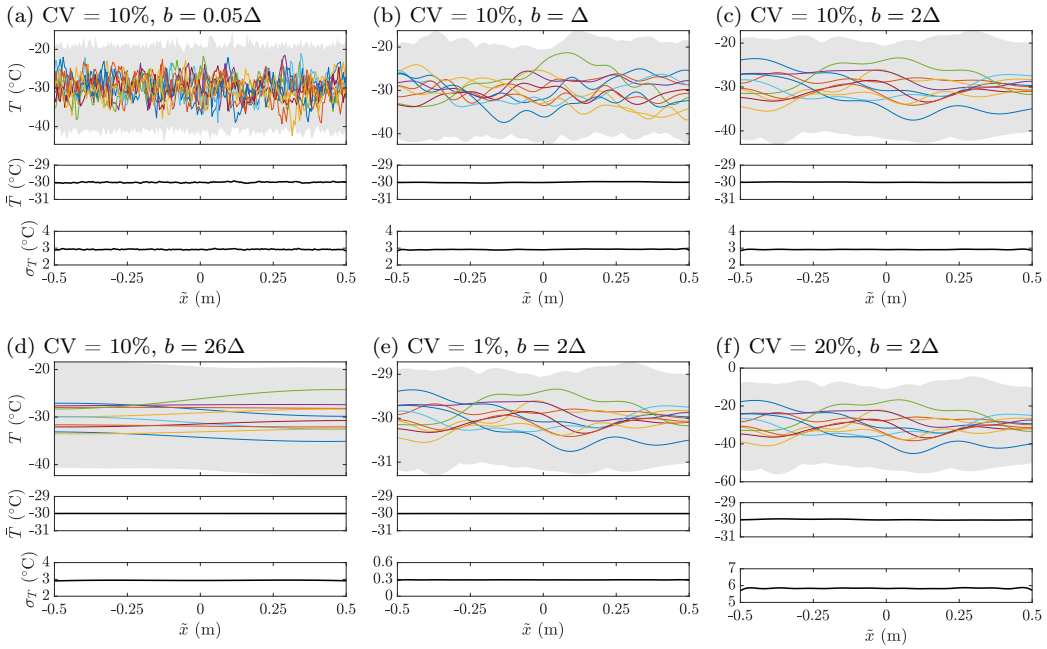


Figure 9: Envelopes of 10000 samples of the temperature random field shaded in gray, and some arbitrarily chosen samples, together with related statistics (means and standard deviations), under different combinations of b and CV.

Young's modulus. However, since $E^{(\mathrm{e})}(x, \theta)$ is linearly related to temperature according to Eq. (16), sampling data similar to those presented above are omitted here for the random Young's modulus.

The probabilistic characterizations shown in Fig. 10 suggest that all distributions have roughly symmetrical shapes, with skewness values close to zero. Similarly to results in Fig. 5, all distributions in Fig. 10 have slightly longer left tails, which is supported by the negative skewness values. It is also apparent that all PDFs are slightly steep, sustained by the kurtosis values varying from 3.03 to 3.07. In addition, the mean value of all distributions are exactly 9.29 kN, which is very close to the mean values of the stochastic axial forces shown in Fig. 5.

Regarding the influence of the parameters of the random field, the most apparent observation is that the dispersion of the axial force, indicated by σ_N, depends not only on the CV assigned to the input random variables, but also on the correlation length b. The influence of this later, for a fixed CV of 10%, can be observed in Figs. 10a–10d, which show that σ_N exhibits a

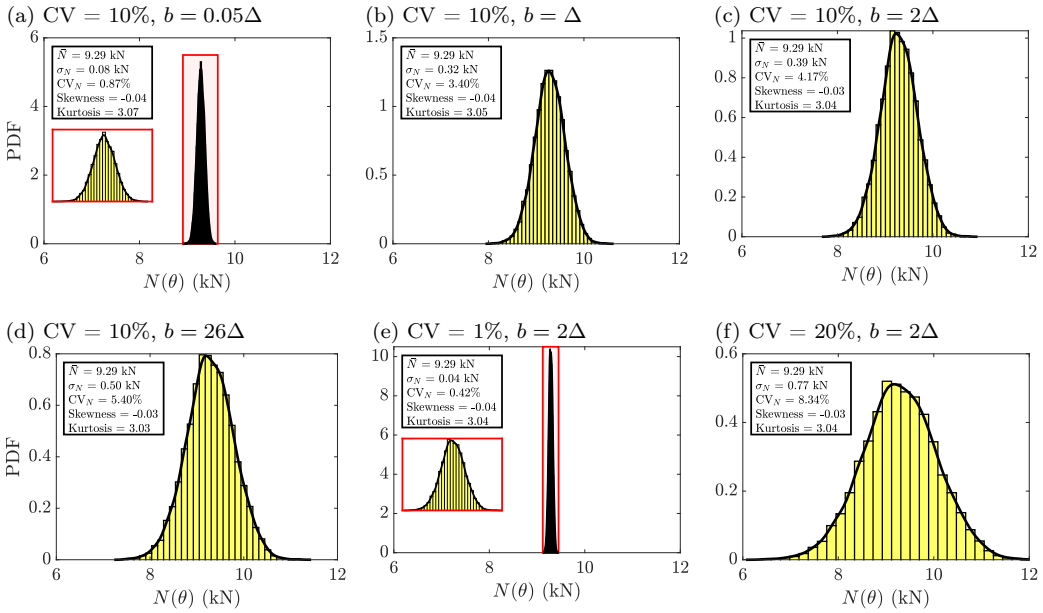


Figure 10: Histograms, PDFs, and statistics related to the stochastic axial force, for different combinations of b and CV, solely accounting for environmental randomness while maintaining the mean values assigned to all spring stiffnesses.

nonlinear monotonic increase for increasing values of b. On the other hand, the influence of CV on the standard deviation of the stochastic axial force, for a fixed b of 2Δ, can be assessed through Figs. 10e, 10c, and 10f, in which σ_N is seen to increase in an approximate linear monotonic way for increasing values of CV assigned to the input random variables.

After introducing the temperature random field samples in Fig. 9, and understanding the randomnesses in the stochastic axial force showed in Fig. 10, uncertainty propagation is performed through the calculations of transmissibility functions, using Eq. (26). Therefore, Fig. 11 shows, shaded in gray, the envelopes for all samples of the transmissibility curves, which were computed for the input and output locations shown in Fig. 4b, and also some arbitrarily chosen samples. Each row and column of Fig. 11 corresponds to a fixed value of b and CV, respectively, encompassing all combinations of the values set for both parameters.

Close to results shown previously, in Fig. 6, Fig. 11 reveals that the increased level of uncertainty assigned to the temperature random field, corresponding to increasing values of CV, results in narrower attenuation bands,

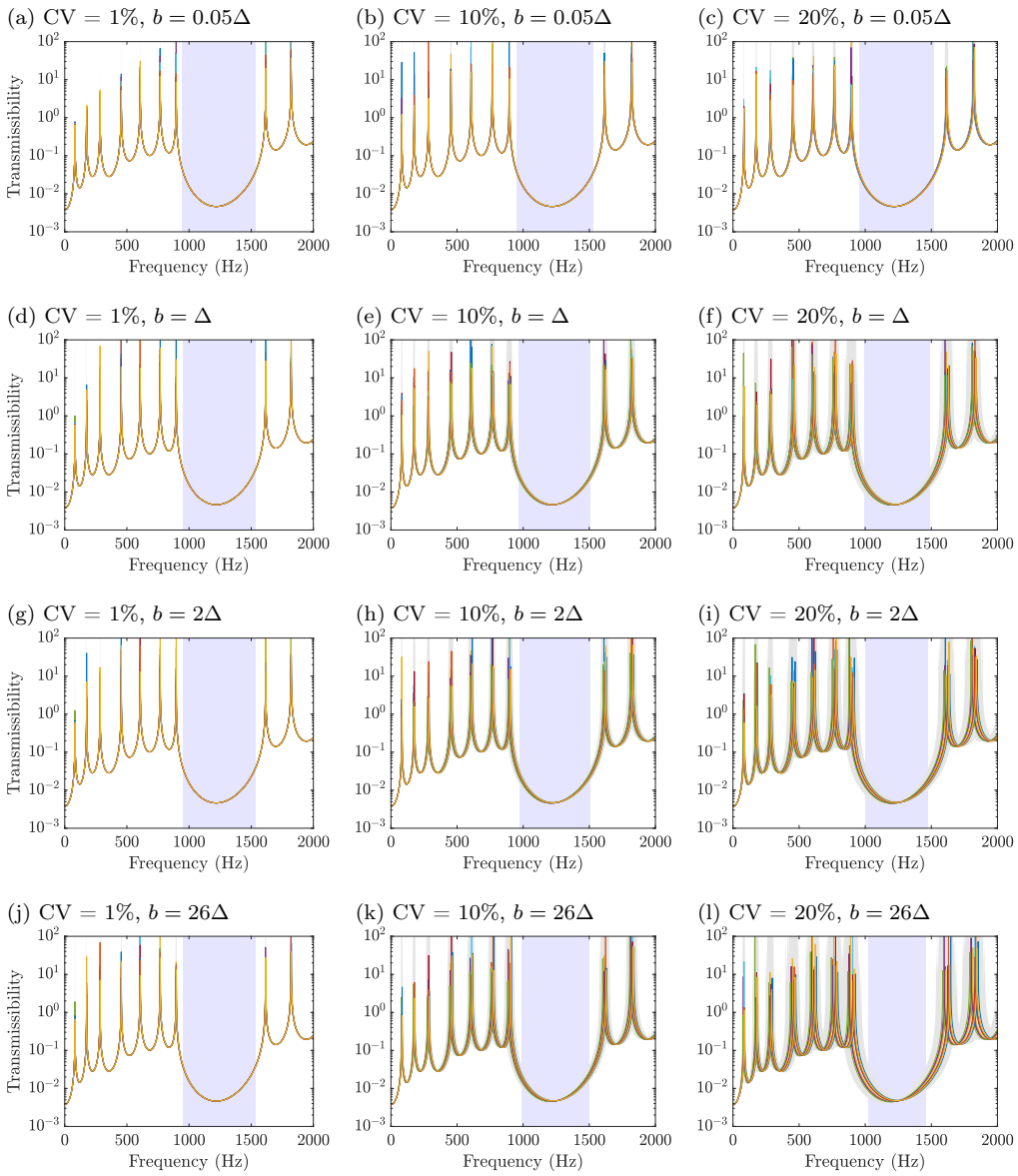


Figure 11: Envelopes of all 10000 samples of transmissibility curves $\mathrm{T}_{(3,159)}$ shaded in gray, and some arbitrarily selected transmissibility samples, solely accounting for environmental randomness while maintaining the mean values assigned to all spring stiffnesses. Shaded purple rectangular regions indicate the intersection of stop bands of all samples.

as clearly demonstrated by the NABs, indicated by the shaded purple rectangular regions. This trend can be better seen from the second row onward

of Fig. 11, since the changes only slightly affect the dynamic behavior of the periodic beam when $b \to 0$ ($b = 0.05\Delta$).

Regarding the influence of the correlation length, for all cases, an increase in b also causes a decrease in the width of the intersection region between attenuation bands identified for each sample. Thus, a scenario of higher variability can be potentiated for large values of b. This pattern is more evident in the second and third columns of Fig. 11. Further clarifications regarding the influence of b on the beam dynamics are provided later on.

From the MC transmissibility function samples, whose envelopes were depicted in Fig. 11, histograms, fitted PDFs, and associated statistics have been computed for the bandgap characteristics. Figure 12 initially shows data related to the bandgap central frequency. In Figs. 12a–12d, the effect of the correlation length on the bandgap central frequency can be assessed, for a fixed CV of 10%, while Figs. 12e, 12c, and 12f enables to appraise the impact of varying CV on the bandgap central frequencies at a fixed correlation length value $b = 2\Delta$. Note that these results correspond to data obtained from transmissibility curves in the second column and third row of Fig. 11.

As one may observe in Fig. 12, the distributions of the bandgap central frequency are visually close to Gaussian, which is supported by the skewness and kurtosis values computed for each case. When the correlation length increases, for a fixed CV of 10%, the data become more disperse with respect to the mean central frequency of approximately 1239 Hz, as confirmed by the nonlinear increase in standard deviation values. On the other hand, as one might expect, Figs. 12e, 12c and 12f reveal that the level of randomness attributed to the temperature random field is linearly related to the dispersion of the bandgap central frequency (cf. $\sigma_{f_{\text{central}}}$).

Statistics regarding the bandgap bandwidth are presented in Fig. 13 for the same combinations of CVs and correlation lengths considered previously in Fig. 12. In general, the conclusions drawn from the results presented in Fig. 13 are similar to those regarding the bandgap central frequency in Fig. 12. Therefore, the distributions depicted in Fig. 13 resemble Gaussian ones, as supported by their skewness and kurtosis values close to 0 and 3, respectively. Additionally, the results in Figs. 13a–13d indicate that $\sigma_{f_{\text{width}}}$ increases monotonically in a nonlinear manner with respect to b, while it is linearly amplified with increasing values of CV for a fixed correlation length of 2Δ, as shown in Figs. 13e, 13c and 13f.

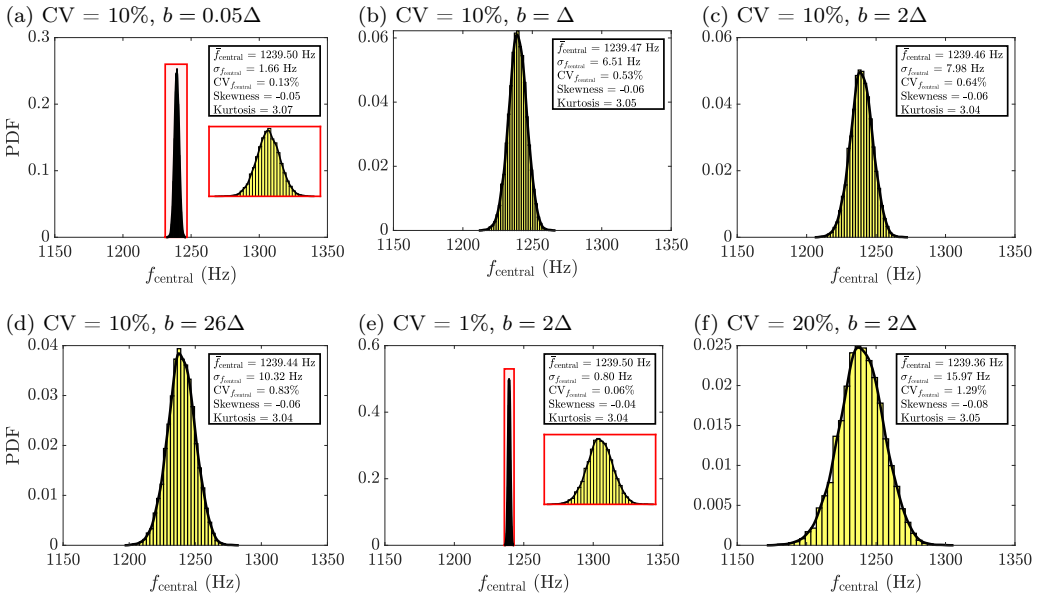


Figure 12: Histograms, PDFs, and statistical measures of central frequency distributions for different CVs and correlation lengths for the input random variables, solely accounting for environmental randomness while maintaining the mean values assigned to all spring stiffnesses.

3.5. Combined randomness in boundary conditions and temperature

The previous two subsections examined separately the significance of accounting for the effects of thermal and BCs randomness on the dynamic behavior of a periodic beam. Cases where these two sources of uncertainty are concurrent, which is likely in many practical applications, are now examined. In Subsection 3.5.1, statistical data related to the stochastic axial force are presented. Subsequently, in Subsection 3.5.2, transmissibilities computed through MC simulations are used for the calculation of PDFs and histograms concerning the central frequency position and width of the investigated attenuation band. Results similar to those presented in Figs. 6 and 11 are omitted for the sake of brevity. In Subsection 3.5.3, reliability analysis is conducted considering different values of the limiting frequencies determining the serviceability limits of the beam. Finally, sensitivity analyses with respect to the bandgap central frequency and width, involving all random variables, are performed in Subsection 3.5.4.

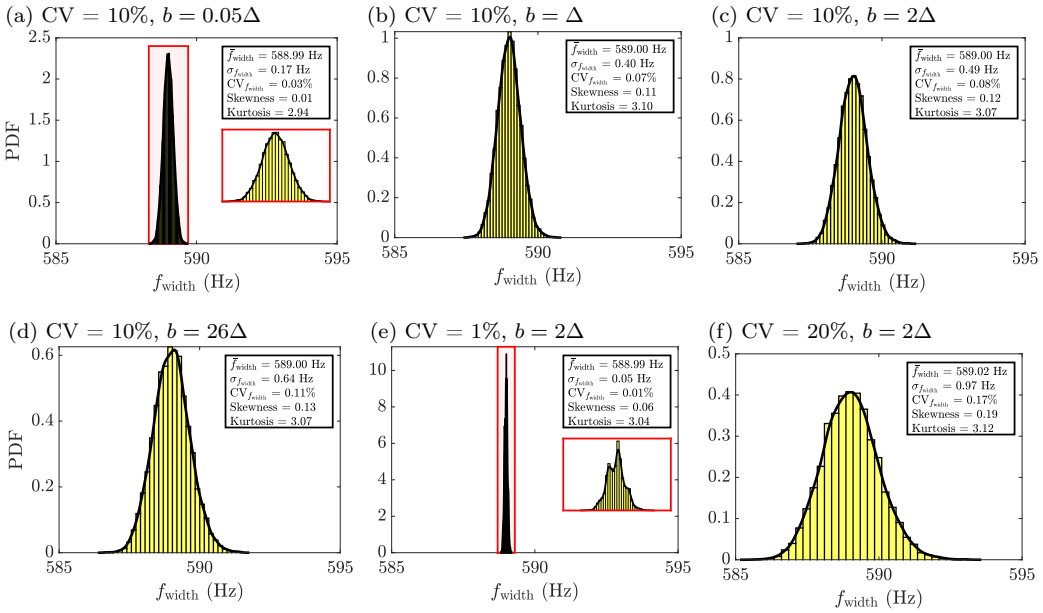


Figure 13: Histograms, PDFs, and statistical measures of bandwidth distributions for different CVs and correlation lengths for the input random variables, solely accounting for environmental randomness while maintaining the mean values assigned to all spring stiffnesses.

3.5.1. PDFs and statistics estimated for the stochastic axial force

Using the temperature random field samples previously introduced in Subsection 3.4 (cf. Fig. 9), the corresponding values of the stochastic axial forces have been calculated considering also stochastic axial spring coefficients, following Eq. (20). Figure 14 shows the histograms, fitted PDFs and statistics for the same combinations of b and CV as those used in Fig. 10. It should be pointed-out that, in each case, the same value of CV is assigned to the random boundary stiffnesses and temperature field.

Similarly to the results reported previously, Fig. 14 reveals that all distributions of the stochastic axial force have shapes close to that of Gaussian distributions (cf. the skewness and kurtosis values, which are approximately 0 and 3, respectively). Their mean values correspond to approximately 9.28 kN. In addition, Figs. 14a–14d show that the standard deviation of the stochastic axial force has a nonlinear relationship with respect to correlation length of the temperature field. As b increases, σ_N exhibits a monotonically increasing trend, as found in Fig. 10. Conversely, Figs. 14e, 14c, and 14f show that

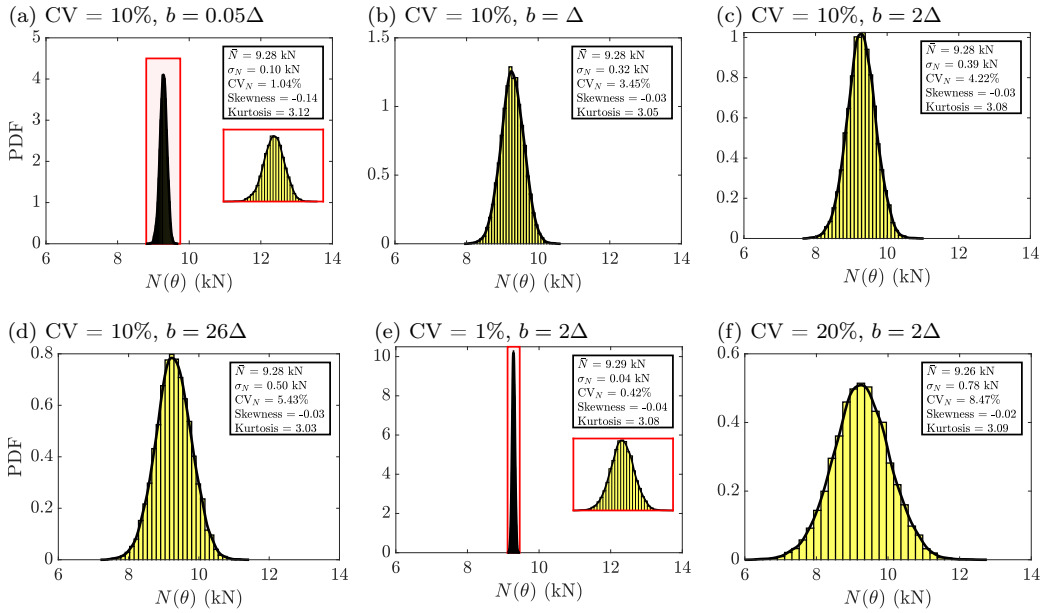


Figure 14: Histograms, PDFs, and statistics related to the stochastic axial force, for different CVs and correlation lengths for the input random variables, accounting for environmental uncertainties and randomness in BCs.

σ_N exhibits a linear relationship with the values of CV assigned to the input random variables, which differs from the results in Fig. 5, where a nonlinear relationship between CV and σ_N was found for the case that one considered the randomness only in the BCs while maintaining the temperature field with the mean value $\bar{T} = -30°\text{C}$.

3.5.2. PDFs of the central frequency and bandwidth of the attenuation band

The probabilistic features of the stochastic attenuation bands, accounting for randomness in BCs and temperature field are presented in Figs. 15 and 16 for the stop band central frequency and bandwidth, respectively.

First, as one notices in Fig. 15, the histograms exhibit strong symmetry and distributions that resemble Gaussian ones. This is evident from the shape of the resulting distributions and the values of kurtosis, which are close to 3, and skewness, which are near 0. In addition, for a fixed CV of 10% assigned to the input random variables, Figs. 15a–15d show that the standard deviation of the output random variable, $\sigma_{f_{\text{central}}}$, exhibits a nonlinear relationship with the values of b assigned to the temperature random field. Nonetheless, for a fixed b, the relationship between the input CV and the output standard

deviation $\sigma_{f_{\text{central}}}$ is approximately linear, cf. Figs. 15e, 15c, and 15f.

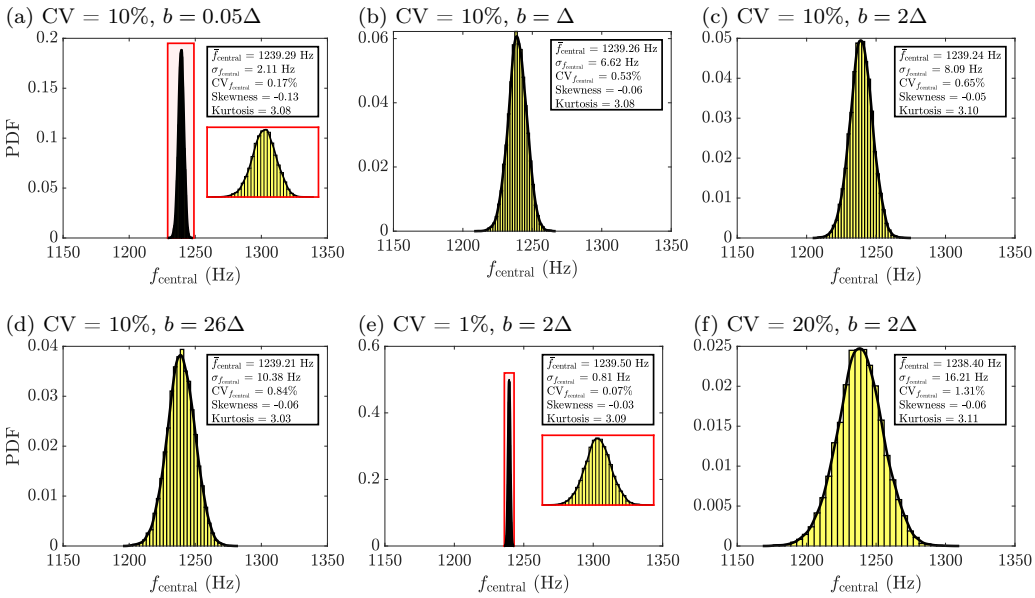


Figure 15: Histograms, PDFs, and statistics of the bandgap central frequency distributions for different CVs and correlation lengths for the input random variables, accounting for environmental uncertainties and randomness in BCs.

On the other hand, distributions depicted in Fig. 16 for the bandgap width are no longer close to Gaussian, except for the case shown in Fig. 16e, where kurtosis and skewness values are close to those shown in Fig. 15. This similarity is explained by the low level of uncertainty assigned to the input random variables, i.e., CV = 1%. In the asymmetric distributions, one notices that the left tail is longer than the right one. Moreover, from Fig. 16, one notices that CV and b show, respectively, a quasi-linear and nonlinear relationship with $\sigma_{f_{\text{width}}}$, as found for the central frequency distribution in Fig. 15.

The results in Figs. 7, 12, and 15 fully characterize the central frequency of bandgaps calculated for the nominally periodic beam while accounting for environmental and BC effects individually or simultaneously. In summary, the randomness in BCs has shown a nonlinear effect on the characterization of f_{central} in Fig. 7, whereas environmental random sources affecting the beam's Young's modulus exhibited nonlinear and linear behaviors with b and CV, respectively, in Fig. 12. When both sources of uncertainties are combined, f_{central} still follows a nonlinear behavior with b in Fig. 15. However,

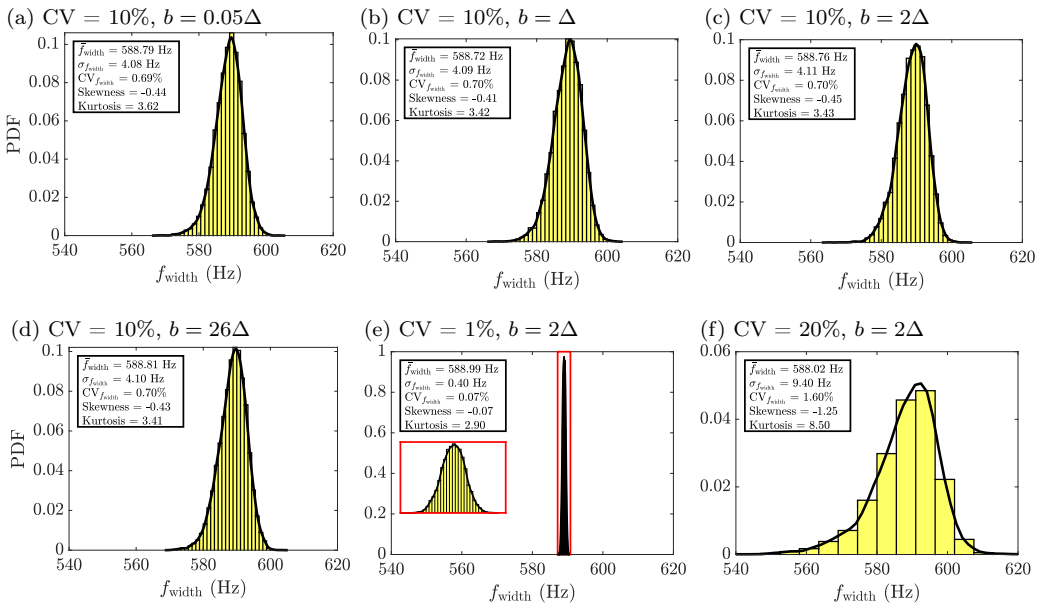


Figure 16: Histograms, PDFs, and statistical measures of bandwidth distributions for different CVs and correlation lengths for the input random variables, accounting for environmental uncertainties and randomness in BCs.

it exhibits an approximately linear behavior with respect to CV, attributed to BC effects. Uncertainty quantification of the bandgap width distribution f_{width} was illustrated in Figs. 8, 13, and 16, revealing the same trends as observed for the central frequency of bandgaps, as presented in Figs. 7, 12, and 15 and discussed just before.

The variability of the main features of the attenuation band (central frequency and bandwidth) for the three cases considered previously, can be further appraised by examining the mean values, standard deviations and CVs presented in Tabs. 1 and 2. From the first of these tables, it can be seen that, for the attenuation band central frequency f_{central}, the variability due to temperature randomness is more significant than those in BCs, and the combined effects of these two sources of uncertainty are always larger than their individual effects. Also evident in Tab. 1 is the strong impact of the correlation length of the temperature random field on the variability of the central frequency.

On the other hand, Tab. 2 illustrates the opposite behavior regarding the variability of the bandgap bandwidth f_{width}. This stochastic parameter is

Table 1: Mean, standard deviation and CV values for the attenuation band central frequency, considering the isolated effects of randomnesses in BCs and temperature field, and their combined influences.

Randomness in BCs						
CV (%)	1	10	20			
$\bar{f}_{\text{central}}$(Hz)	1239.50	1239.29	1238.57			
$\sigma_{f_{\text{central}}}$(Hz)	0.12	1.28	2.92			
$\text{CV}_{f_{\text{central}}}$ (%)	0.01	0.10	0.24			
Randomness in temperature field						
CV (%)	10				1	20
b (m)	0.05Δ	Δ	2Δ	26Δ	2Δ	2Δ
$\bar{f}_{\text{central}}$(Hz)	1239.50	1239.47	1239.46	1239.44	1239.50	1239.36
$\sigma_{f_{\text{central}}}$(Hz)	1.66	6.51	7.98	10.32	0.80	15.97
$\text{CV}_{f_{\text{central}}}$ (%)	0.13	0.53	0.64	0.83	0.06	1.29
Combined randomness in BCs and temperature field						
CV (%)	10				1	20
b (m)	0.05Δ	Δ	2Δ	26Δ	2Δ	2Δ
$\bar{f}_{\text{central}}$(Hz)	1239.29	1239.26	1239.24	1239.21	1239.50	1238.40
$\sigma_{f_{\text{central}}}$(Hz)	2.11	6.62	8.09	10.38	0.81	16.21
$\text{CV}_{f_{\text{central}}}$ (%)	0.17	0.53	0.65	0.84	0.07	1.31

mostly influenced by randomness in BCs rather than uncertainties from temperature fluctuations. Naturally, the combined effects of these two sources of uncertainty always surpass their individual effects, as observed previously for the bandgap central frequency in Tab. 1. Table 2 also highlights that the correlation length of the temperature random field has a minor effect on the variability of the attenuation bandwidth.

It is worthy commenting that the rather small values of $\sigma_{f_{\text{central}}}$, $\text{CV}_{f_{\text{central}}}$, $\sigma_{f_{\text{width}}}$, and $\text{CV}_{f_{\text{width}}}$ shown in Tabs. 1 and 2 could be interpreted as indicating negligible influence of the uncertainties considered on the features of the attenuation band. In this regard, it is important to notice that: a) the values of the above-mentioned output statistics have been obtained for the specific values of the parameters CV and b considered in the calculations. Should these values be different in other cases of interest, higher (or lower) values of the output statistics would be obtained; b) despite the small values of output statistics, the variability affecting the features of the attenuation band can have significant influence on the robustness of the periodic beam. This is clearly demonstrated in the next section in which a sampling-based reliability assessment is performed.

Table 2: Mean, standard deviation and CV values for the attenuation bandwidth considering the isolated effects of randomnesses in BCs and temperature field and their combined influences.

Randomness in BCs						
CV (%)	1	10	20			
$\bar{f}_{\text{width}}$ (Hz)	588.99	588.81	588.13			
$\sigma_{f_{\text{width}}}$ (Hz)	0.39	4.06	9.27			
$\text{CV}_{f_{\text{width}}}$ (%)	0.07	0.69	1.58			
Randomness in temperature field						
CV (%)	10				1	20
b (m)	0.05Δ	Δ	2Δ	26Δ	2Δ	2Δ
$\bar{f}_{\text{width}}$ (Hz)	588.89	589.00	589.00	589.00	588.89	589.02
$\sigma_{f_{\text{width}}}$ (Hz)	0.17	0.40	0.49	0.64	0.05	0.97
$\text{CV}_{f_{\text{width}}}$ (%)	0.03	0.07	0.08	0.11	0.01	0.17
Combined randomness in BCs and temperature field						
CV (%)	10				1	20
b (m)	0.05Δ	Δ	2Δ	26Δ	2Δ	2Δ
$\bar{f}_{\text{width}}$ (Hz)	588.79	588.72	588.76	588.81	588.99	588.02
$\sigma_{f_{\text{width}}}$ (Hz)	4.08	4.09	4.11	4.10	0.40	9.40
$\text{CV}_{f_{\text{width}}}$ (%)	0.69	0.70	0.70	0.70	0.07	1.60

3.5.3. Reliability analysis

Reliability is defined here as the probability of the attenuation band encompassing the interval defined between two limiting design frequencies, $f_{\text{L}d}$ and $f_{\text{R}d}$. It is evaluated for different pairs of values of these two later, chosen in the frequency band of interest. From the samples extracted from the transmissibility functions, for each pair of limiting values, the reliability can be calculated as the ratio n_c/N_s, where n_c is the number of samples satisfying the tested condition, and N_s is the total number of samples (which equals 10000 in the present study).

Figure 17 illustrates the reliability values, calculated for the same CV and b values considered before, plotted against various design bandgaps. The influence of b, for a fixed CV, can be appraised in Figs. 17a–17d, whereas Figs. 17e, 17c, and 17f illustrate the impact of CV, for a fixed b. It should be mentioned that, for all cases depicted in Fig. 17, the first design bandgap, with the lowest reliability value, corresponds to the mean bandgap of the beam, defined previously in Subsection 3.2, i.e., $f_{\text{L}d} = f_{\text{L}} = 945\,\text{Hz}$ and $f_{\text{R}d} = f_{\text{R}} = 1534\,\text{Hz}$.

In particular, Figs. 17a–17d show that larger values of b tend to reduce

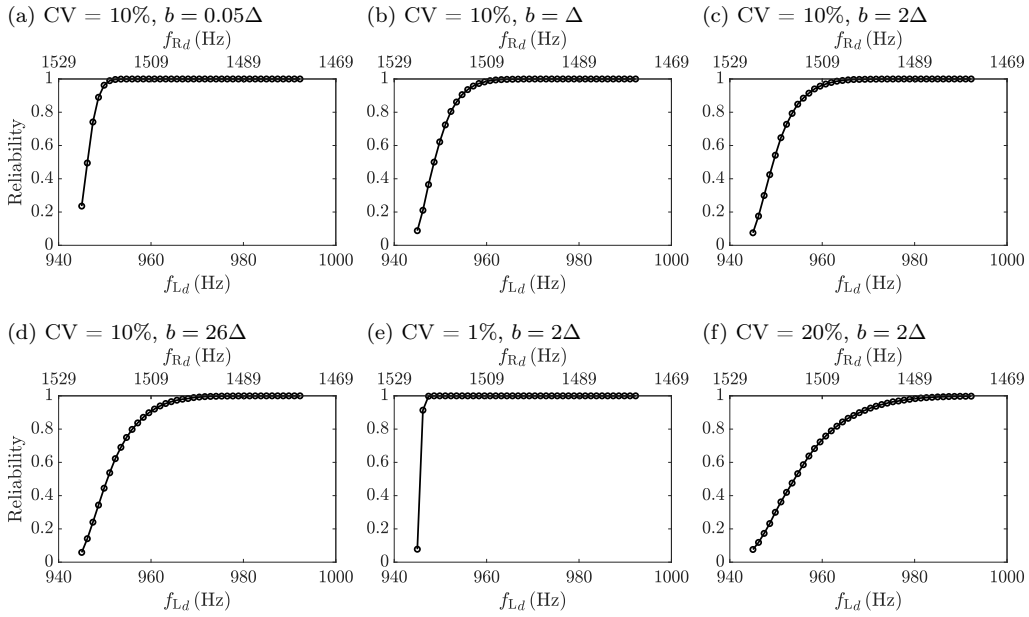


Figure 17: Reliability values for different CVs and correlation lengths for the input random variables, accounting for environmental uncertainties and randomness in BCs.

the reliability, due to the increasing variability in the temperature random field, cf. Fig. 9. It can also be observed that the reliability values depend on the limiting frequencies defining the design bandgap. As $f_{\mathrm{L}d}$ increases and $f_{\mathrm{R}d}$ decreases, the reliability grows, owing to the narrower band specified for the design bandgap. Regarding the influence of the CV, Figs. 17e, 17c, and 17f indicate that the reliability decreases with increasing values of CV assigned to the input random variables, while keeping the correlation length fixed. It is also noticeable that the reliabilities are strongly dependent on the bandwidth of the design bandgap as well.

Lastly, Tab. 3 presents the reliability values calculated for the periodic beam considering all combinations of b and CV, taking into account the isolated effects of randomnesses in BCs and the temperature field, as well as their combined influences, for a design bandgap defined within the band $f_{\mathrm{L}d} = 1.01 \times f_{\mathrm{L}} \approx 992\,\mathrm{Hz}$ and $f_{\mathrm{R}d} = 0.99 \times f_{\mathrm{R}} \approx 1457\,\mathrm{Hz}$. The results in Tab. 3 clearly show that when the CV is very low, defined as CV = 1%, the effects of all randomnesses are negligible for the investigated design bandgap. However, the reliability values decrease considerably with increasing variability affecting the dynamic behavior of the beam. Additionally, Tab. 3 further il-

lustrates the significant impact of correlation length on the reliability values, demonstrating its critical role in the overall uncertainty quantification process. In the worst-case scenario, when the combined randomnesses in BCs and the temperature field are considered, for CV = 20% and $b = 26\Delta$, a reliability of 0.43 is found, which is too low for most, if not all, engineering applications. The shown results indicate that environmental and BCs uncertainties should not be neglected when investigating the dynamic behavior of periodic structures, for their impact on features of interest, such as bandgaps, can be relevant. Notwithstanding, one is also able to confirm observations already provided, i.e., when input random quantities are characterized by low values of CV, they do not significantly influence characteristics of the considered attenuation band, for the analyzed periodic beam.

Table 3: Reliability values for different CVs and correlation lengths for the input random variables, considering the isolated effects of randomnesses in BCs and temperature field, as well as their combined influences, for a design bandgap ranging from $f_{\mathrm{L}d} = 1.01 \times f_{\mathrm{L}} \approx 992\,\mathrm{Hz}$ to $f_{\mathrm{R}d} = 0.99 \times f_{\mathrm{R}} \approx 1457\,\mathrm{Hz}$.

	Randomness in BCs	Randomness in temperature field				Combined randomness in BCs and temperature field			
		$b\,(\mathrm{m})$							
CV (%)		0.05Δ	Δ	2Δ	26Δ	0.05Δ	Δ	2Δ	26Δ
1	1	1	1	1	1	1	1	1	1
10	0.99	1	0.91	0.85	0.75	0.99	0.90	0.84	0.74
20	0.96	0.99	0.65	0.56	0.45	0.94	0.60	0.52	0.43

3.5.4. Sensitivity analyses

Sensitivity analyses are conducted here to quantify the relative influence of each random variable in the stochastic model, including temperature variations and non-ideal BCs, on the two parameters defining the attenuation band. Ideally, these analyses could precede uncertainty propagation by MC simulations, aiming to filter out less significant random variables from the stochastic model, thereby accelerating computations in subsequent analyses. However, the main interest here is to compute sensitivities as a complementary means of interpreting the results obtained in the previous subsections and, more specifically, to assess the adequacy of the criterion suggested in [32] for selecting the most relevant random variables for KL expansions, as discussed previously, in Subsection 3.1.

One first recalls that the temperature random field was represented by employing KL expansion, for which $N = 340$, 18, 10, and 2 random variables were adopted for $b = 0.05\Delta$, Δ, 2Δ, and 26Δ, respectively. On the other hand, variabilities regarding non-ideal BCs were modeled by means of $k_x^{\mathrm{L}}(\theta)$, $k_y^{\mathrm{L}}(\theta)$, $k_\beta^{\mathrm{L}}(\theta)$, $k_x^{\mathrm{R}}(\theta)$, $k_y^{\mathrm{R}}(\theta)$, and $k_\beta^{\mathrm{R}}(\theta)$ stochastic quantities. Therefore, for each correlation length, a total of 346, 24, 16, and 8 random variables were involved.

Based on the theory provided in Subsection 2.4 and referring to Eqs. (27)-(29), let $g \equiv f_{\mathrm{central}}$ and subsequently $g \equiv f_{\mathrm{width}}$, so that the sensitivity indices $(S^{\sigma}_{f_{\mathrm{central}}})^2$ and $(S^{\sigma}_{f_{\mathrm{width}}})^2$ are computed for each random variable. As the same value of CV is applied simultaneously to all variables in each analysis, the sensitivity indices are independent from the level of uncertainty assigned to the input random variables. Therefore, the choice of CV for performing such computations is arbitrary.

Accordingly, Fig. 18 shows sensitivity indices calculated for the bandgap characteristics of the nominally periodic beam, i.e., its central frequency and bandwidth. Furthermore, since a large number of random variables are required to properly describe the random field when $b \to 0$, only the first four squared sigma-normalized relations related to the KL expansion are shown separately, for convenience. The remaining random variables, except those associated with BCs, are exhibited in groups of 120.

As evident from Fig. 18a, variabilities in f_{central} are predominantly influenced by uncertainties related to temperature variations. When $b \to 0$, the central frequency position of the attenuation band can be slightly influenced by some higher-order KL random variables, while in the limit as $b \to \infty$, f_{central} appears to be entirely governed by ξ_1. Concerning the variabilities of the bandwidth, Fig. 18b illustrates that the spring stiffness k_y^{L} governs the width of the attenuation bands for all values of the correlation length. Smaller sensitivity indices, though non-negligible, are observed for k_y^{R}. This is attributed to the asymmetry of the unit cell chosen in this study (cf. Fig. 1). Furthermore, given that the transmissibility curves were computed in the y-direction while applying a harmonic excitation in the same direction, the outcomes presented in Fig. 18b are consistent with expectations. Specifically, the spring stiffnesses in the y-direction exert a more significant impact on the beam's response, as could be anticipated.

Furthermore, these results closely align with outcomes from Tabs. 1 and 2. In both cases, it is clear that environmental randomness plays the most significant role in determining the bandgap central frequency f_{central}, whereas

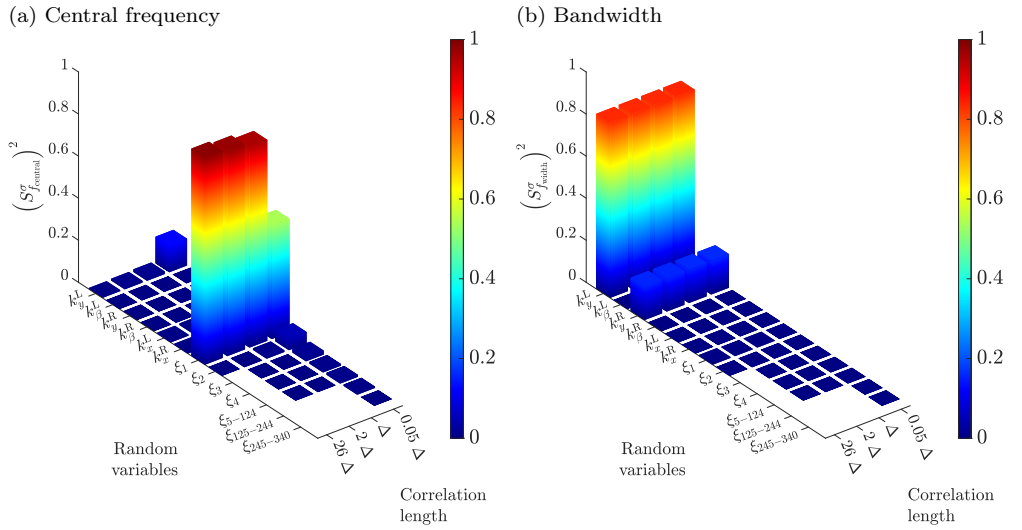


Figure 18: Sensitivity analyses for the central frequency and bandwidth of the beam's stop bands for $b = 0.05\Delta$, Δ, 2Δ, and 26Δ, accounting for environmental uncertainties and randomness in BCs.

BC uncertainties mostly affect the bandgap bandwidth f_{width}. This result further emphasizes the need of simultaneously considering multiple sources of uncertainties when designing and analyzing periodic structures — as neglecting some of them, even unknowingly, might harm predictions, potentially implying in nonconformity regarding design requirements, due to a lack of robustness against variability.

Lastly, it should also be noted that the sensitivity values depicted in Fig. 18 are in disagreement with the criterion established in [32] for retaining the most significant random variables for the temperature random field. However, if a reduced number of random variables were used to discretize the random field, following the sensitivity analysis method as proposed in [32], proper spatial representation of the temperature random field, as seen previously in Fig. 9a, for example, might have not been achieved.

4. Summary and concluding remarks

In this article, a stochastic model accounting for randomness in temperature and BCs has been proposed, aiming at investigating the influence of such randomness on the attenuation band characteristics of periodic beams, i.e., its central frequency and bandwidth. Despite being based on classical

UQ techniques (KL expansion and MC simulations), the proposed stochastic model features the novelty of combining the two sources of uncertainty for the prediction of dynamic responses, for which a novel formulation has been developed. In this regard, temperature fluctuations are considered to affect the material properties and also engender random thermal stresses. Additionally, the uncertain BCs have been considered to affect both the axial and bending dynamic behavior of the beam, as well as to influence thermal stresses and the clamp configuration. Various scenarios characterized by different values of the key properties of the input random quantities (namely, the coefficients of variation of the random variables and random fields, CVs, and the correlation length of the random field, b) have been examined. The results obtained enabled to evaluate the separate influences of each source of uncertainty and also their combined effect on the beam's dynamic behavior. The results show that the variability of the attenuation band features is governed not only by the value of CVs of the input random quantities (which is frequently regarded as a preferred metric for random dispersion), but also by the correlation length of the random temperature fluctuations, which drives the space-dependent correlation between the random variables represented by the random field. Numerical simulations revealed that the bandgap central frequency stochastic response is primarily influenced by the variability of the random temperature field, while the bandgap bandwidth has been shown to be mostly affected by the random inputs related to the uncertain BCs. Although low CV and standard deviation values have been obtained for the dispersion of the bandgap features, reliability analyses have been performed, revealing low reliability values for some designs. Additionally, greater correlation lengths and CVs for the input random quantities have led to increased variability in both the bandgap central frequency and bandwidth. In summary, the overall conclusion is that uncertainties affecting temperature and BCs, which are likely to happen in real-world situations, can exert significant influences on the dynamic responses of periodic beams, and should be considered in the analysis and design of such structures.

Acknowledgments

The authors are grateful to the Brazilian Coordination for the Improvement of Higher Education Personnel (CAPES), the Brazilian National Council for Scientific and Technological Development (CNPq), and the São Paulo Research Foundation (FAPESP) for their continued support to the authors'

works. In particular, the authors acknowledge FAPESP for the thematic grant #18/15894-0, related to the "Periodic structure design and optimization for enhanced vibroacoustic performance: ENVIBRO" research project. V. M. S. Santos acknowledges FAPESP for the grants #2023/11207-7 and #2024/07549-2. D. A. Rade acknowledges CNPq (grant #312068/2020-4) and FAPESP (grant #2021/11258-5, project FLYMOV) for the financial support to his research work.

References

[1] F. Liang, Y. Chen, J.-J. Gong, Y. Qian, Vibration self-suppression of spinning fluid-conveying pipes composed of periodic composites, Int. J. Mech. Sci. 220 (2022) 107150. doi:10.1016/j.ijmecsci.2022.107150.

[2] Z. Jiang, Y. Zhou, S. Zheng, J. Liu, B. Xia, Waveguides induced by replacing defects in phononic crystal, Int. J. Mech. Sci. 255 (2023) 108464. doi:10.1016/j.ijmecsci.2023.108464.

[3] R. Z. Zhang, Y. Cong, M. Sellam, A. Chpoun, Bandgap analysis of periodic composite plates considering fluid-structure coupling, J. Sound Vib. 582 (2024) 118412. doi:10.1016/j.jsv.2024.118412.

[4] Muhammad, W. Zhou, C. W. Lim, Topological edge modeling and localization of protected interface modes in 1D phononic crystals for longitudinal and bending elastic waves, Int. J. Mech. Sci. 159 (2019) 359–372. doi:10.1016/j.ijmecsci.2019.05.020.

[5] L. Tang, L. Cheng, Periodic plates with tunneled Acoustic-Black-Holes for directional band gap generation, Mech. Syst. Signal Pr. 133 (2019) 106257. doi:10.1016/j.ymssp.2019.106257.

[6] Z. Alam, S. Padmanabhan, A. K. Sharma, Magnetically tunable longitudinal wave band gaps in hard-magnetic soft laminates, Int. J. Mech. Sci. 249 (2023) 108262. doi:10.1016/j.ijmecsci.2023.108262.

[7] D. Z. Li, S. P. Li, N. N. Ma, H. M. Wang, C. L. Zhang, W. Q. Chen, Propagation characteristics of elastic longitudinal wave in a piezoelectric semiconductor metamaterial rod and its tuning, Int. J. Mech. Sci. 266 (2024) 108977. doi:10.1016/j.ijmecsci.2024.108977.

[8] M. I. Hussein, M. J. Leamy, M. Ruzzene, Dynamics of Phononic Materials and Structures: Historical Origins, Recent Progress, and Future Outlook, Appl. Mech. Rev. 66 (2014) 040802. doi:10.1115/1.4026911.

[9] P. A. Deymier, Acoustic Metamaterials and Phononic Crystals, 1 ed., Springer Berlin, Heidelberg, 2013.

[10] Y.-F. Wang, Y.-Z. Wang, B. Wu, W. Chen, Y.-S. Wang, Tunable and Active Phononic Crystals and Metamaterials, Appl. Mech. Rev. 72 (2020) 040801. doi:10.1115/1.4046222.

[11] N. Gao, Z. Zhang, J. Deng, X. Guo, B. Cheng, H. Hou, Acoustic Metamaterials for Noise Reduction: A Review, Adv. Mater. Technol. 7 (2022) 2100698. doi:10.1002/admt.202100698.

[12] S. S. Mester, H. Benaroya, Periodic and Near-periodic Structures, Shock Vib. 2 (1995) 69–95. doi:10.1155/1995/392839.

[13] R. S. Langley, Wave transmission through one-dimensional near periodic structures: optimum and to random disorder, J. Sound Vib. 188 (1995) 717–743. doi:10.1006/jsvi.1995.0620.

[14] H. Benaroya, Waves in periodic structures with imperfections, Compos. B: Eng. 28 (1997) 143–152. doi:10.1016/s1359-8368(96)00025-x.

[15] W. Gao, Z. Qin, F. Chu, Broadband vibration suppression of rainbow metamaterials with acoustic black hole, Int. J. Mech. Sci. 228 (2022) 107485. doi:10.1016/j.ijmecsci.2022.107485.

[16] Y. Wang, W. Zhang, On the thermal buckling and postbuckling responses of temperature-dependent graphene platelets reinforced porous nanocomposite beams, Compos. Struct. 296 (2022) 115880. doi:10.1016/j.compstruct.2022.115880.

[17] F. Mohd, M. Talha, Influence of material uncertainties on thermomechanical postbuckling behaviour of graphene reinforced functionally graded porous beams, Acta Mech. Sin. 39 (2023) 722385. doi:10.1007/s10409-022-22385-x.

[18] D. J. Mead, Vibration and buckling of flat free-free plates under non-uniform in-plane thermal stresses, J. Sound Vib. 260 (2003) 141–165. doi:10.1016/s0022-460x(02)00919-7.

[19] Y. Chen, B. Wu, Y. Su, W. Chen, Effects of strain stiffening and electrostriction on tunable elastic waves in compressible dielectric elastomer laminates, Int. J. Mech. Sci. 176 (2020) 105572. doi:10.1016/j.ijmecsci.2020.105572.

[20] R. F. Gibson, Principles of Composite Material Mechanics, CRC Press, Boca Raton, 2016.

[21] U. Lee, J. Kim, Determination of Nonideal Beam Boundary Conditions: A Spectral Element Approach, AIAA J. 38 (2000) 309–316. doi:10.2514/2.958.

[22] B. Huang, Q. S. Li, W. H. Shi, Z. Wu, Eigenvalues of structures with uncertain elastic boundary restraints, Appl. Acoust. 68 (2007) 350–363. doi:10.1016/j.apacoust.2006.01.012.

[23] R. A. Ibrahim, C. L. Pettit, Uncertainties and dynamic problems of bolted joints and other fasteners, J. Sound Vib. 279 (2005) 857–936. doi:10.1016/j.jsv.2003.11.064.

[24] M. Dilena, M. F. Dell'Oste, A. Morassi, Crack identification in rods and beams under uncertain boundary conditions, Int. J. Mech. Sci. 133 (2017) 651–661. doi:10.1016/j.ijmecsci.2017.09.017.

[25] N. J. Lindsley, C. L. Pettit, P. S. Beran, Nonlinear plate aeroelastic response with uncertain stiffness and boundary conditions, Struct. Infrastruct. E. 2 (2006) 201–220. doi:10.1080/15732470600590564.

[26] J. D. Reid, N. R. Hiser, Detailed modeling of bolted joints with slippage, Finite Elem. Anal. Des. 41 (2005) 547–562. doi:10.1016/j.finel.2004.10.001.

[27] M. Tabaddor, Influence of nonlinear boundary conditions on the single-mode response of a cantilever beam, Int. J. Solids Struct. 37 (2000) 4915–4931. doi:10.1016/s0020-7683(99)00197-3.

[28] M. Claeys, J.-J. Sinou, J.-P. Lambelin, B. Alcoverro, Multi-harmonic measurements and numerical simulations of nonlinear vibrations of a beam with non-ideal boundary conditions, Commun. Nonlinear Sci. Numer. Simul. 19 (2014) 4196–4212. doi:10.1016/j.cnsns.2014.04.008.

[29] T. Roncen, J.-J. Sinou, J.-P. Lambelin, Non-linear vibrations of a beam with non-ideal boundary conditions and uncertainties – Modeling, numerical simulations and experiments, Mech. Syst. Signal Pr. 110 (2018) 165–179. doi:10.1016/j.ymssp.2018.03.013.

[30] Y. Feng, D. Wu, M. G. Stewart, W. Gao, Past, current and future trends and challenges in non-deterministic fracture mechanics: A review, Comput. Method. Appl. M. Eng. 412 (2023) 116102. doi:10.1016/j.cma.2023.116102.

[31] J.-M. Mencik, N. Bouhaddi, Dynamic reanalysis of structures with geometric variability and parametric uncertainties via an adaptive model reduction method, Mech. Syst. Signal Pr. 190 (2023) 110127. doi:10.1016/j.ymssp.2023.110127.

[32] R. C. Smith, Uncertainty Quantification: Theory, Implementation, and Applications, SIAM - Society for Industrial and Applied Mathematics, Philadelphia, 2013.

[33] R. Ghanem, D. Higdon, H. Owhadi, Handbook of Uncertainty Quantification, Springer Cham, Gewerbestrasse, 2017.

[34] M. Zhang, Q. Wang, Z. Luo, W. Gao, Stochastic bandgap optimization for multiscale elastic metamaterials with manufacturing imperfections, Int. J. Mech. Sci. 268 (2024) 109035. doi:10.1016/j.ijmecsci.2024.109035.

[35] L. H. M. S. Ribeiro, C. Claeys, A. T. Fabro, D. Chronopoulos, J. R. F. Arruda, Robust optimization of a 3D printed periodic frame structure using the inferred characterization of the additive manufacturing system, Mech. Syst. Signal Pr. 217 (2024) 111515. doi:10.1016/j.ymssp.2024.111515.

[36] H. Al Ba'ba'a, S. Nandi, T. Singh, M. Nouh, Uncertainty quantification of tunable elastic metamaterials using polynomial chaos, J. Appl. Phys. 127 (2020). doi:10.1063/1.5130685.

[37] N. Korshunova, I. Papaioannou, S. Kollmannsberger, D. Straub, E. Rank, Uncertainty quantification of microstructure variability and mechanical behavior of additively manufactured lattice structures,

Comput. Method. Appl. M. Eng. 385 (2021) 114049. doi:10.1016/j.cma.2021.114049.

[38] A. T. Fabro, H. Meng, D. Chronopoulos, Uncertainties in the attenuation performance of a multi-frequency metastructure from additive manufacturing, Mech. Syst. Signal Pr. 138 (2020) 106557. doi:10.1016/j.ymssp.2019.106557.

[39] M. R. Souza, D. Beli, N. S. Ferguson, J. R. de F. Arruda, A. T. Fabro, A bayesian approach for wavenumber identification of metamaterial beams possessing variability, Mech. Syst. Signal Pr. 135 (2020) 106437. doi:10.1016/j.ymssp.2019.106437.

[40] T. Chatterjee, D. Karličić, S. Adhikari, M. I. Friswell, Gaussian process assisted stochastic dynamic analysis with applications to near-periodic structures, Mech. Syst. Signal Pr. 149 (2021) 107218. doi:10.1016/j.ymssp.2020.107218.

[41] G. Agrawal, A. Gupta, R. Chowdhury, A. Chakrabarti, Robust topology optimization of negative Poisson's ratio metamaterials under material uncertainty, Finite Elem. Anal. Des. 198 (2022) 103649. doi:10.1016/j.finel.2021.103649.

[42] Z. Li, L. Wang, G. Xinyu, A double-layer mesh-driven robust topology optimization strategy for mechanical metamaterials under size uncertainty, Thin-Walled Struct. 196 (2024) 111439. doi:10.1016/j.tws.2023.111439.

[43] Z. Li, L. Wang, X. Geng, W. Chen, B. Han, Complex uncertainty-oriented robust topology optimization for multiple mechanical metamaterials based on double-layer mesh, Comput. Method. Appl. M. Eng. 419 (2024) 116589. doi:10.1016/j.cma.2023.116589.

[44] L. H. M. S. Ribeiro, V. F. Dal Poggetto, J. R. F. Arruda, Robust optimization of attenuation bands of three-dimensional periodic frame structures, Acta Mech. 233 (2022) 455–475. doi:10.1007/s00707-021-03118-x.

[45] G. S. Sharma, B. Faverjon, D. Dureisseix, A. Skvortsov, I. MacGillivray, C. Audoly, N. Kessissoglou, Acoustic Performance

of a Periodically Voided Viscoelastic Medium With Uncertainty in Design Parameters, J. Vib. Acoust. 142 (2020) 061002. doi:10.1115/1.4046859.

[46] K. Modur, G. S. Sharma, C. Lin, N. Wendt, A. Skvortsov, I. MacGillivray, N. Kessissoglou, Uncertainty quantification for locally resonant coated plates and shells, Int. J. Mech. Sci. 282 (2024) 109587. doi:10.1016/j.ijmecsci.2024.109587.

[47] T. Chatterjee, D. Karličić, M. Cajić, S. Adhikari, M. I. Friswell, Uncertainty quantification in inerter-based quasiperiodic lattices, Int. J. Mech. Sci. 249 (2023) 108258. doi:10.1016/j.ijmecsci.2023.108258.

[48] R. Santoro, M. Mazzeo, G. Failla, A computational framework for uncertain locally resonant metamaterial structures, Mech. Syst. Signal Pr. 190 (2023) 110094. doi:10.1016/j.ymssp.2023.110094.

[49] R. P. Singh, C. Droz, M. Ichchou, F. Franco, O. Bareille, S. De Rosa, Stochastic wave finite element quadratic formulation for periodic media: 1D and 2D, Mech. Syst. Signal Pr. 136 (2020) 106431. doi:10.1016/j.ymssp.2019.106431.

[50] M. Ma, L. Wang, Reliability-based topology optimization framework of two-dimensional phononic crystal band-gap structures based on interval series expansion and mapping conversion method, Int. J. Mech. Sci. 196 (2021) 106265. doi:10.1016/j.ijmecsci.2020.106265.

[51] P. Greengard, M. O'Neil, Efficient reduced-rank methods for Gaussian processes with eigenfunction expansions, Stat. Comput. 32 (2022) 94. doi:10.1007/s11222-022-10124-z.

[52] C. Soize, Uncertainty Quantification, Springer Cham, Gewerbestrasse, 2017.

[53] A. T. Fabro, N. S. Ferguson, B. R. Mace, Structural vibration analysis with random fields using the hierarchical finite element method, J. Braz. Soc. Mech. Sci. Eng. 41 (2019) 80. doi:10.1007/s40430-019-1579-0.

[54] E. Bahmyari, Free and forced vibration analysis of moderately thick plates with uncertain material properties using the Chaotic Radial

Basis Function, Eng. Anal. Boundary Elem. 106 (2019) 349–358. doi:10.1016/j.enganabound.2019.04.035.

[55] R. G. Ghanem, P. D. Spanos, Stochastic Finite Elements: A Spectral Approach, Springer, New York, 1991.

[56] J. Son, Y. Du, An Efficient Polynomial Chaos Expansion Method for Uncertainty Quantification in Dynamic Systems, Appl. Mech. 2 (2021) 460–481. doi:10.3390/applmech2030026.

[57] C. Scarth, S. Adhikari, P. H. Cabral, G. H. C. Silva, A. P. d. Prado, Random field simulation over curved surfaces: Applications to computational structural mechanics, Comput. Method. Appl. M. Eng. 345 (2019) 283–301. doi:10.1016/j.cma.2018.10.026.

[58] A. Mohammadi, M. Raisee, Stochastic field representation using bi-fidelity combination of proper orthogonal decomposition and Kriging, Comput. Method. Appl. M. Eng. 357 (2019) 112589. doi:10.1016/j.cma.2019.112589.

[59] G. Hemanth, K. J. Vinoy, S. Gopalakrishnan, Spectral Stochastic Finite Element Method for Periodic Structure, in: IEEE Int. Microw. RF Conf., IEEE, 2014, pp. 9–12. doi:10.1109/imarc.2014.7038959.

[60] T. Mukhopadhyay, S. Adhikari, A. Batou, Frequency domain homogenization for the viscoelastic properties of spatially correlated quasi-periodic lattices, Int. J. Mech. Sci. 150 (2019) 784–806. doi:10.1016/j.ijmecsci.2017.09.004.

[61] R. A. Borges, L. F. F. Rodovalho, T. P. Sales, D. A. Rade, Stochastic eigenfrequency and buckling analyses of plates subjected to random temperature distributions, Mech. Syst. Signal Pr. 147 (2021) 107088. doi:10.1016/j.ymssp.2020.107088.

[62] A. Haldar, S. Mahadevan, Probability, Reliability, and Statistical Methods in Engineering Design, John Wiley & Sons, NY, 2000.

[63] H. Peng, F. Sun, F. Wu, D. Yang, Dynamic reliability of mechanism based on direct probability integral method, Int. J. Mech. Sci. 270 (2024) 109105. doi:10.1016/j.ijmecsci.2024.109105.

[64] M. Zhang, Q. Wang, Z. Luo, W. Gao, Virtual model-aided reliability analysis considering material and geometrical uncertainties for elastic metamaterials, Mech. Syst. Signal Pr. 211 (2024) 111199. doi:10.1016/j.ymssp.2024.111199.

[65] A. F. Russillo, V. G. Kouznetsova, G. Failla, M. G. D. Geers, A reduced-order computational homogenization framework for locally resonant metamaterial structures, Comput. Mech. (2024). doi:10.1007/s00466-024-02453-9.

[66] L. H. Ribeiro, V. F. Dal Poggetto, C. Claeys, D. Chronopoulos, J. R. Arruda, Computing dispersion diagrams and forced responses of arbitrarily varying waveguides, Int. J. Mech. Sci. 258 (2023) 108540. doi:10.1016/j.ijmecsci.2023.108540.

[67] G. Stefanou, The stochastic finite element method: Past, present and future, Comput. Methods Appl. Mech. Eng. 198 (2009) 1031–1051. doi:10.1016/j.cma.2008.11.007.

[68] D. Xiu, Numerical Methods for Stochastic Computations: A Spectral Method Approach, Princeton University Press, Princeton, 2010. doi:10.1515/9781400835348.

[69] M. Kamiński, The Stochastic Perturbation Method for Computational Mechanics, John Wiley & Sons, Chichester, 2013. doi:10.1002/9781118481844.

[70] J. N. Reddy, Introduction to the Finite Element Method, McGraw-Hill Education, New York, 2018.

[71] M. R. Eslami, R. B. Hetnarski, J. Ignaczak, N. Noda, N. Sumi, Y. Tanigawa, Theory of Elasticity and Thermal Stresses: Explanations, Problems and Solutions, Springer, Dordrecht, 2013.

[72] A. Batou, C. Soize, Stochastic modeling and identification of an uncertain computational dynamical model with random fields properties and model uncertainties, Arch. Appl. Mech. 83 (2012) 831–848. doi:10.1007/s00419-012-0720-7.

[73] S. Cantero-Chinchilla, A. T. Fabro, H. Meng, W.-J. Yan, C. Papadimitriou, D. Chronopoulos, Robust optimised design of 3D printed elastic

metastructures: A trade-off between complexity and vibration attenuation, J. Sound Vib. 529 (2022) 116896. doi:10.1016/j.jsv.2022.116896.

[74] S. Bi, M. Beer, S. Cogan, J. Mottershead, Stochastic model updating with uncertainty quantification: An overview and tutorial, Mech. Syst. Signal Pr. 204 (2023) 110784. doi:10.1016/j.ymssp.2023.110784.

[75] A. T. Fabro, H. Meng, D. Chronopoulos, Correlated disorder in rainbow metamaterials for vibration attenuation, Proc. Inst. Mech. Eng. C 235 (2021) 2610–2621. doi:10.1177/0954406220986596.

[76] J. R. Davis, Aluminum and Aluminum Alloys, ASM International, Chagrin Falls, 1993.

[77] C. Mapelli, A. Manes, M. Giglio, D. Mombelli, C. Baldizzone, A. Gruttadauria, Microstructural investigation on an Al 6061 T6 alloy subjected to ballistic impact, Procedia Eng. 10 (2011) 3447–3452. doi:10.1016/j.proeng.2011.04.568.

[78] R. A. Yildiz, S. Yilmaz, Stress-Strain Properties of Artificially Aged 6061 Al Alloy: Experiments and Modeling, J. Mater. Eng. Perform. 29 (2020) 5764–5775. doi:10.1007/s11665-020-05080-6.

[79] J. E. Jensen, R. G. Stewart, W. A. Tuttle, H. Brechna, Selected Cryogenic Data Notebook: Sections I-IX, Technical Report DEAC0276CH00016, Brookhaven National Laboratory, United States Department of Energy, 1980.

[80] P. Foteinopoulos, A. Papacharalampopoulos, P. Stavropoulos, On thermal modeling of Additive Manufacturing processes, CIRP J. Manuf. Sci. Technol. 20 (2018) 66–83. doi:10.1016/j.cirpj.2017.09.007.

[81] NIST, Aluminum 6061-T6 (UNS AA96061), 2018. URL: https://www.nist.gov/mml/acmd/aluminum-6061-t6-uns-aa96061, [accessed 06 December 2022].

[82] D. Duhamel, B. R. Mace, M. J. Brennan, Finite element analysis of the vibrations of waveguides and periodic structures, J. Sound Vib. 294 (2006) 205–220. doi:10.1016/j.jsv.2005.11.014.

[83] Y. Waki, B. R. Mace, M. J. Brennan, Numerical issues concerning the wave and finite element method for free and forced vibrations of waveguides, J. Sound Vib. 327 (2009) 92–108. doi:10.1016/j.jsv.2009.06.005.

[84] B. R. Mace, D. Duhamel, M. J. Brennan, L. Hinke, Finite element prediction of wave motion in structural waveguides, J. Acoust. Soc. Am. 117 (2005) 2835–2843. doi:10.1121/1.1887126.

[85] Y. E. Lage, M. M. Neves, N. M. M. Maia, D. Tcherniak, Force transmissibility versus displacement transmissibility, J. Sound Vib. 333 (2014) 5708–5722. doi:10.1016/j.jsv.2014.05.038.

[86] R. R. Craig, A. J. Kurdila, Fundamentals of Structural Dynamics, John Wiley & Sons, Hoboken, 2011.

[87] A. Saltelli, S. Tarantola, F. Campolongo, M. Ratto, Sensitivity Analysis in Practice: A Guide to Assessing Scientific Models, volume 1, John Wiley & Sons, Chichester, 2004.

[88] B. Sudret, Uncertainty propagation and sensitivity analysis in mechanical models – Contributions to structural reliability and stochastic spectral methods, Ph.D. thesis, Université Blaise Pascal - Clermont II, 2007.

[89] A. Saltelli, M. Ratto, T. Andres, F. Campolongo, J. Cariboni, D. Gatelli, M. Saisana, S. Tarantola, Global Sensitivity Analysis. The Primer, John Wiley & Sons, Chichester, 2008.

[90] E. Borgonovo, E. Plischke, Sensitivity analysis: A review of recent advances, Eur. J. Oper. Res. 248 (2016) 869–887. doi:10.1016/j.ejor.2015.06.032.

[91] D. Marques, D. Vandepitte, V. Tita, Sensitivity and uncertainty analysis for structural health monitoring with crack propagation under random loads: A numerical framework in the frequency domain, Fatigue Fract. Eng. Mater. Struct. 46 (2022) 137–152. doi:10.1111/ffe.13853.

[92] C. Fu, J.-J. Sinou, W. Zhu, K. Lu, Y. Yang, A state-of-the-art review on uncertainty analysis of rotor systems, Mech. Syst. Signal Pr. 183 (2023) 109619. doi:10.1016/j.ymssp.2022.109619.

[93] S. Razavi, A. Jakeman, A. Saltelli, C. Prieur, B. Iooss, E. Borgonovo, E. Plischke, S. Lo Piano, T. Iwanaga, W. Becker, S. Tarantola, J. H. Guillaume, J. Jakeman, H. Gupta, N. Melillo, G. Rabitti, V. Chabridon, Q. Duan, X. Sun, S. Smith, R. Sheikholeslami, N. Hosseini, M. Asadzadeh, A. Puy, S. Kucherenko, H. R. Maier, The future of sensitivity analysis: an essential discipline for systems modeling and policy support, Environ. Model. Softw. 137 (2021) 104954. doi:10.1016/j.envsoft.2020.104954.

[94] S.-K. Choi, R. A. Canfield, R. V. Grandhi, Reliability-based Structural Design, Springer, London, 2007.

[95] B. Staber, J. Guilleminot, A random field model for anisotropic strain energy functions and its application for uncertainty quantification in vascular mechanics, Comput. Method. Appl. M. Eng. 333 (2018) 94–113. doi:10.1016/j.cma.2018.01.001.

[96] J. Guilleminot, A. Asadpoure, M. Tootkaboni, Topology optimization under topologically dependent material uncertainties, Struct. Multidiscip. O. 60 (2019) 1283–1287. doi:10.1007/s00158-019-02247-1.

[97] S. Chu, J. Guilleminot, Stochastic multiscale modeling with random fields of material properties defined on nonconvex domains, Mech. Res. Commun. 97 (2019) 39–45. doi:10.1016/j.mechrescom.2019.01.008.

[98] B. Staber, J. Guilleminot, C. Soize, J. Michopoulos, A. Iliopoulos, Stochastic modeling and identification of a hyperelastic constitutive model for laminated composites, Comput. Method. Appl. M. Eng. 347 (2019) 425–444. doi:10.1016/j.cma.2018.12.036.

[99] S. Chu, J. Guilleminot, C. Kelly, B. Abar, K. Gall, Stochastic Modeling and identification of material parameters on structures produced by additive manufacturing, Comput. Method. Appl. M. Eng. 387 (2021) 114166. doi:10.1016/j.cma.2021.114166.

[100] Z. Zheng, M. Beer, U. Nackenhorst, An iterative multi-fidelity scheme for simulating multi-dimensional non-Gaussian random fields, Mech. Syst. Signal Pr. 200 (2023) 110643. doi:10.1016/j.ymssp.2023.110643.

[101] H. Kim, M. D. Shields, Modeling strongly non-Gaussian non-stationary stochastic processes using the Iterative Translation Approximation Method and Karhunen-Loève expansion, Comput. Struct. 161 (2015) 31–42. doi:10.1016/j.compstruc.2015.08.010.

[102] H. Parviz, M. Fakoor, Free vibration of a composite plate with spatially varying Gaussian properties under uncertain thermal field using assumed mode method, Physica A Stat. Mech. Appl. 559 (2020) 125085. doi:10.1016/j.physa.2020.125085.

[103] H. Parviz, M. Fakoor, Stochastic free vibration of composite plates with temperature-dependent properties under spatially varying stochastic high thermal gradient, Mech. Based Des. Struc. 51 (2021) 5878–5901. doi:10.1080/15397734.2021.2014863.

[104] H. Parviz, M. Fakoor, F. Hosseini, Probabilistic thermal stability of laminated composite plates with temperature-dependent properties under a stochastic thermal field, Acta Mech. 233 (2022) 1351–1370. doi:10.1007/s00707-022-03167-w.

[105] National Research Council, The airliner cabin environment and the health of passengers and crew, National Academies Press, Washington DC, 2002. doi:10.17226/10238.

[106] Z. Huda, P. Edi, Materials selection in design of structures and engines of supersonic aircrafts: A review, Mater. Des. 46 (2013) 552–560. doi:10.1016/j.matdes.2012.10.001.

[107] M. Tesón, M. J. González-García, A. López-Miguel, A. Enríquez-de Salamanca, V. Martín-Montañez, M. J. Benito, M. E. Mateo, M. E. Stern, M. Calonge, Influence of a Controlled Environment Simulating an In-Flight Airplane Cabin on Dry Eye Disease, Invest. Ophthalmol. Vis. Sci. 54 (2013) 2093–2099. doi:10.1167/iovs.12-11361.

[108] X. Cao, C. D. Zevitas, J. D. Spengler, B. Coull, E. McNeely, B. Jones, S. M. Loo, P. MacNaughton, J. G. Allen, The on-board carbon dioxide concentrations and ventilation performance in passenger cabins of US domestic flights, Indoor Built Environ. 28 (2018) 761–771. doi:10.1177/1420326x18793997.

[109] M. B. Hermansen, J. J. Thomsen, Vibration-based estimation of beam boundary parameters, J. Sound Vib. 429 (2018) 287–304. doi:10.1016/j.jsv.2018.05.016.

[110] J. Carneiro Jr, M. Brennan, P. Gonçalves, V. Cleante, D. Bueno, R. Santos, On the attenuation of vibration using a finite periodic array of rods comprised of either symmetric or asymmetric cells, J. Sound Vib. 511 (2021) 116217. doi:10.1016/j.jsv.2021.116217.

[111] The MathWorks Inc., std, 2024. URL: https://www.mathworks.com/help/matlab/ref/std.html, [accessed 27 August 2024].

[112] The MathWorks Inc., skewness, 2024. URL: https://www.mathworks.com/help/stats/skewness.html, [accessed 27 August 2024].

[113] The MathWorks Inc., kurtosis, 2024. URL: https://www.mathworks.com/help/stats/kurtosis.html, [accessed 27 August 2024].